Parkinsonian resting tremor

Source and Interaction with Movement

by

Piergiuseppe Liuzzi

to obtain the degree of Master of Science
at the Delft University of Technology,
to be defended publicly on Friday September 11, 2020.

Student number: 4925629
Thesis committee:
Dr. Ir. M. Negrello, TU Delft, supervisor
Dr. Ir. W. Mugge, TU Delft, supervisor
Dr. Ir. A. Schouten, TU Delft, supervisor
Dr. Ir. R. C. Hendriks, TU Delft, external committee member

TU Delft

Preface

This basis for this research originally stemmed from my passion for the brain. As Lyall Watson states: *if the brain were so simple we could understand it, we would be so simple we couldn't*. This thesis is the first step of my life towards contradicting this statement. We are not simple and our brain is not simple, and only through centuries of studies and research we can face the complexity inside us. Conversely to what Lyall says, I think we have the capabilities to understand the working principles of our brain, we only need the chances to do it.

This work has been made possible by the NMC lab and by Mario Negrello, which combined, allowed me to walk on a path a bit aside from my studies enlarging my horizon and my views. Thank you all for your unwavering support.

Acknowledgements

Foremost, I would like to express my gratitude to my daily supervisor Dr. Mario Negrello for the continuous support during the writing of my thesis. Not only it has been an advisor for the brain, but it has been a friend and an advisor for the heart. I could not have imagined a better mentor and supervisor. This was the confirmation I needed to keep on researching in the near future.

A sincere thanks goes to Dr. Winfred Mugge and Dr. Alfred Schouten, which, even considering the complexity of this period, allowed me to work on what I love giving me guidance and supervision.

I thank my mum and my dad, who are always looking at my progress from anywhere they are and helping me through all difficulties. You supported me and encouraged me to unconditionally pursue what I loved and not what I had to do.
You know why I choose the brain, dad.

Thanks to my family, to my uncle Paolo and aunt Lucia, to uncle Peppino and aunt Liliana. You have always shown interest for what I was doing, and it made me understand why it was worth doing it. Thank you.

I would like to thank my friends, for letting me scream and hang up on them, for ignoring the fact that I have not answered at the phone for months, but mainly because after all this, they are still on my side.

And on my side, I have had the stronger power in nature, love. Giving me the strength for working days and nights. Helping me understand why I was doing it and putting me back up when everything seemed lost. Grazie scricciola, for everything.

Piergiuseppe Liuzzi
Delft, August 2020

Parkinsonian resting tremor. Source and interaction with movement.

Piergiuseppe Liuzzi[1], Winfred Mugge[1] and Alfred Schouten[1], Mario Negrello[2]

[1] *NeuroMechanics and Muscular Control Lab, Technische Universiteit Delft, Mekelweg 5, 2628 CD Delft, Netherlands*
[2] *Department of Neuroscience, Erasmus Univeresiteit, Burgemeester Oudlaan 50, 3062 PA Rotterdam, Netherlands*

September 2, 2020

Biologically inspired neural networks are a promising approach to understand the causes and improve the treatments of brain damage. Parkinson's disease is a progressive nervous system disorder that affects mainly movements, speech and cognitive problems. It symptoms cannot be cured, though medications can significantly improve the condition. Among the symptoms, tremor is the only one which remains unaffected by medications and is only responsive to deep-brain stimulation. A simplified, cortico-thalamo-cerebellar model will be simulated with spiking neural networks to evaluate the disease effects under dopamine depletion and connectivity weight changes. Confirming previous findings, striatal dopamine depletion was not found to cause tremor, nor its injection to affect tremor severity. The model showed evidence that parkinsonian weight changes in the pallidal inner feedback loop (GPi-GPe) are responsible of creating a suitable environment for the PD tremor oscillations to rise in the thalamus. Furthermore, both the GPi and the GPe present enhanced maximal activity coherent with muscular co-contraction onsets showing evidence of abnormal basal ganglia firing during re-emergent tremor. These findings may connect abnormal basal ganglia activity to the main parkinsonian motor impairments and may help explaining the beneficial effects of deep-brain stimulation on tremor severity.

1 Introduction

In his 1817 "An essay on the shaking palsy", James Parkinson first described the clinical syndrome that was later to bear his name [1]. Four main features characterize Parkinson Disease (PD): tremor at rest, akinesia, postural instability and rigidity. PD is mainly due to striatal dopamine depletion (DA-D) which relates with all the aforementioned symptoms excluding tremor [2]. Tremor severity, on the other hand, correlates with pallidal DA-D. Furthermore, it has been shown how resting tremor is associated with a different cerebello-thalamic circuit including motor cortex (MC), cerebellum (CBLM), ventral intermediate nucleus of thalamus (VIM) and basal ganglia (BG) [3]. The aforementioned areas have multiple functions, but in our model we will focus on their contribution to motion. Respectively, 1) the MC is responsible of planning, control, and execution of voluntary movements, 2) the CBLM contributes to coordination, precision, and accurate timing by compensating for disturbances, 3) the thalamus relays sensory and motor signals to the cerebral cortex and 4) the BG selects between possible actions in a reinforcement learning manner.
Physiological tremor [4] and essential tremor [5] are found to be influenced by the same circuit. To date, it remains unknown how basal ganglia dysfunctions in PD contributes the VIM-MC-CBLM into generating resting tremor. At the same time, interference with both the BG (subthalamic nucleus [6] and pallidum [7]) and the cerebello-thalamic circuit is shown to

suppress resting tremor [8, 9]. Furthermore, it has been shown that, voluntary movements of limbs tend to interrupt tremor or decrease its severity [10].
In order to understand how and in which node of the circuit this happens, we attempt to model the system via a large scale brain model based on biologically inspired Spiking Neural Networks (SNNs). Three main goals drive implementation decisions: 1) a model in a dynamical-functional framework capable of reproducing prior experimental results, 2) enable a sensitivity analysis of the parameter space of the modeled areas on the kinematic and dynamic variables of a 2-link arm model and resulting tremor bands ($[4-6]\,Hz$) and 3) evaluate the effects of dopamine depletion/injection in both healthy and PD models.
These goals aim to provide hypothesis on the causality of the tremor generation process and quantify the interactive behavior between the illness and the trajectory parameter space.

The neuromechanical model is composed by a 2-link arm model, the motor, sensory and prefrontal cortex, the basal ganglia and the thalamus, the inferior olive (IO) and the Purkinje cells (PCs). We observe a strict relationship between co-contraction and tremor generation. Furthermore, the abnormal activity of GPe-GPi appears to be responsible of excessive synchronization in the basal ganglia, leading to tremor-like dynamics.
In the subsequent sections we describe the anatomy of the system and its modeling counterpart. Results will be provided first for the single areas and then for the totality of the model. Implications of the findings will be subsequently discussed.

2 Materials and Methods

Reaching movements will be performed in a 2D plane through the use of a simplified arm model with forward dynamics simulations. Forward simulation, i.e. providing torques at each time-step, creates an interesting property in the trajectory: in the early phase of the trajectory the contraction is isotonic, while toward the end of the trajectory an isometric contraction appears, because physical constraints such as ligaments present resistance (imagine lifting a weight with your biceps and trying to hyper-flex over the shoulder). This allows for the comparison of the tremor behaviors in two different contraction types, isotonic in the first part and isometric in the second. Golgi Tendon Organs and spindle feedback are modeled using literature results [11, 12, 13, 14].
With a random torques generator, torques are selected and inserted in forward simulations, producing the trajectories dataset. The trajectories dataset are clustered to reduce similar trajectories and to allow for the existence of different reaching paths towards the end-point. The clustered trajectories are then associated with the same endpoint (cluster centroid) and the cortical areas are trained with it respectively to perform: 1) position and force prediction (MC), 2) remap of sensory feedback data into a sufficiently big dimensionality and provide it to the motor cortex (SC) and 3) compute the jerk-minimization principle across the different possible trajectories in a cluster (PFC).

The basal ganglia (GPI, GPE, STN, striatal D1 neurons, striatal D2 neurons) is modeled inspired on the work of T.C. Stewart et al. ([15, 16, 16, 17]) as reinforcement learning based spiking neural architecture which is capable of task selection. Hence dynamically takes the PFC input and converts into a selected action. The thalamus in our model converts the selected action into an utility value. The position and forces from the selected MC module will be used at the next step. The olivocerebellar components are modeled as ensemble arrays of N-dimensional oscillators (IO) and as encoders (PCs). The olivo-cerebellar model is slaved to the rest, hence no compensatory feedback is brought back to the cortical areas. Leaving an open-loop cerebellum is an assumption which slightly reduces the scope of the investigation, but allows for a clearer sensitivity analysis of the parameters in the BG and it does not affect the quality of the results. For technical reasons closed-loop simulations were not conducted given the huge computational time and memory cost. This is due to restarting different neural simulators while freezing the prior time-step parameters at each subsequent step, predict position and force, calculate feedback values, append data for each trajectory with a neural network of more then 26000 neurons. Since it has been proved that the CBLM is not the central pattern generator of PD tremor [18, 19], we can talk of causality in the model in a open-loop sense.
The model is then tested with data from the same distribution, both in its healthy and PD set-up. Furthermore correlational analysis and frequency domain analysis will be performed.
The simulation is discrete with a time step of $dt = 0.005\,s$.

2.1 Trajectories clustering

A 2-dimensional joint space provides simplicity in modeling and good responsiveness to the learning process of neural networks. At the same time, different trajectories might end up in the same end point. In that case, only some of them are optimal, hence chosen by our brain. Clustering allows brain areas as the pre-frontal cortex and the basal ganglia to perform decision making and action selection [20, 21, 22].
In order to do this, a modified version of Nearest Neighbor Clustering (NNC) has been implemented. The modification has been done in order to obtain equal size clusters and provide constant dimensionality to the neural networks (Alg. 1). In the model, each cluster contains $m_{cl} = 10$ trajectories both in the training and in the testing phase. The neuroscientific background

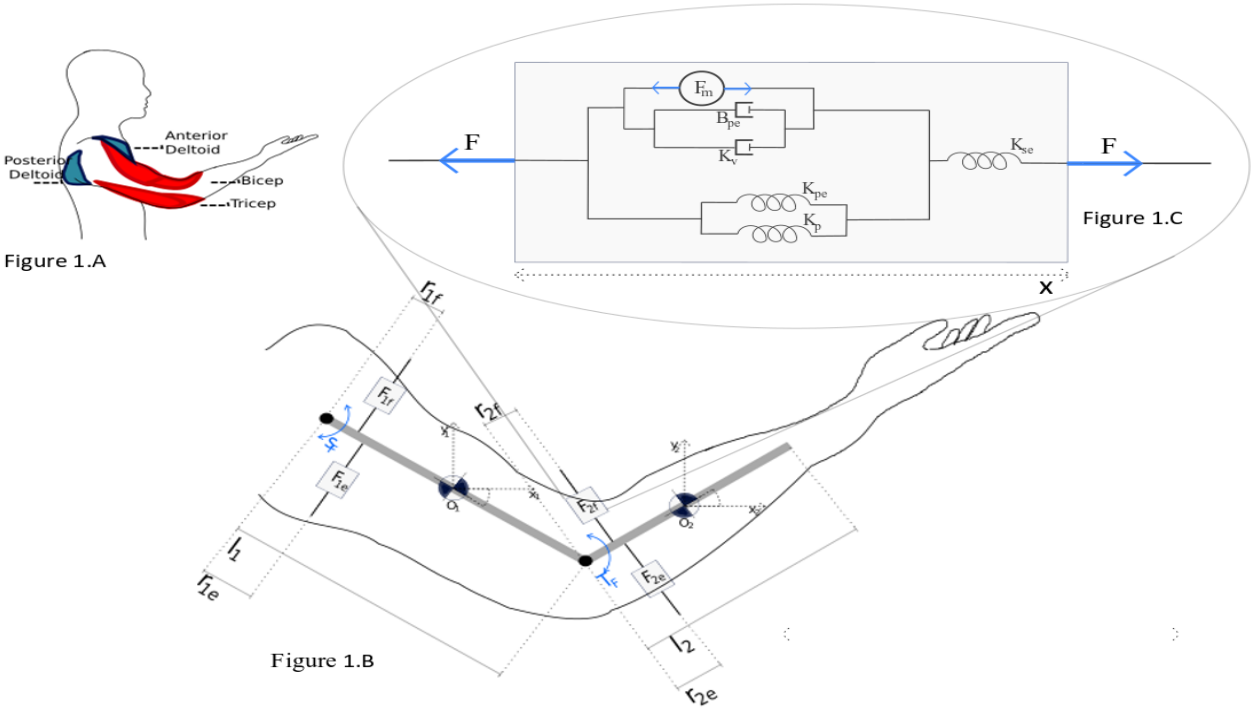

Figure 1: *Fig 1.A: Muscles used for modeling, in red the elbow joint synergy ones and in blue the ones for the shoulder synergy. Fig. 1.B Bio-mechanical modeling of the arm, r is the attachment point distance to the right of the related joint, F is the developed force at the tendon and s_f and e_f are the friction forces opposing the motion. Fig. 1.C: is the Hill muscle model expanded with F_m the active force of the contractile component, K_{pe}, K_{se}, β_{pe} are the muscle stiffness and damping and K_v, K_p the spindle stiffness and damping.*

Calculate euclidean distance matrix;
Create equal random membership;
Compute distance error between endpoints E_0;
while *True* **do**
  $E_p = E_0$;
  forall *a:1:number of endpoint* **do**
    forall *b:1:a* **do**
      Exchange a with b;
      Calculate error E_{ab};
      if $E_{ab} < E_0$ **then**
        $E_0 = E_{ab}$;
      else
        Exchange back b with a;
      end
    end
  end
  if $E_p = E_{ab}$ **then**
    break;
  end
end

Algorithm 1: Equal size clustering algorithm

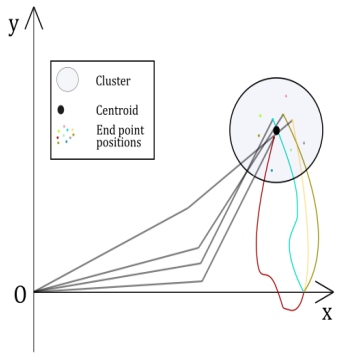

Figure 2: *Representation of clustered trajectories given their hand endpoints.*

behind this, is the theory of *receptive fields*, which is defined as a portion of sensory space that can elicit a precise neuronal response when stimulated. When looking at motor control, the visual system creates receptive fields which are volumes in the visual space. For our purposes, we reduced volumes to 2-dimensional circular areas, hence clusters [23, 24].

2.2 2-Link model

In order to produce the trajectories and feedback values used in the training and test set a 2-link arm model

is used. Both rods possess mass and inertia (Table 1) and they operate in a 2-dimensional joint space in the presence of gravity as seen in (Fig. 1). The movements are performed in the sagittal plane of the arm-model, hence they stay in the X-Y plane of Fig. 1. The equations of motion for the arm are expressed in generalized coordinates $\mathbf{q} = [\theta_1, \theta_2]^T$ w.r.t. the horizontal.
The method used to solve the inverse kinematics is the TMT method [25]. First, the coordinates of the bodies are written as a function of the generalized coordinates $\mathbf{q}$, $\mathbf{x} = \mathbf{T}(\mathbf{q})$ which if derived becomes $\dot{\mathbf{x}_i} = \mathbf{T_i}(q_j)\dot{\mathbf{q}_j}$. Then the reduced mass matrix is computed symbolically with $\bar{\mathbf{M}} = \mathbf{T^T M T}$, hence the name TMT.

$$\bar{\mathbf{Q}} = \bar{\mathbf{M}}\ddot{\mathbf{q}} \tag{1}$$

Eq. 1 is solved in a linear least squares sense obtaining $\ddot{\mathbf{q}}$ which is then integrated for each time step of the simulation. In Eq. 1 the term $\bar{\mathbf{Q}}$ represents the generalized force vector. The mathematical equations used are attached in the supplementary materials section.
The joint friction is expressed by two joint torques s_F and e_F respectively at the shoulder joint and elbow joint.

$$\begin{aligned} s_F &= K_{sh}\theta_1 + \beta_{sh}\dot{\theta_1} \\ e_f &= K_{el}(\theta_2 - \theta_1) + \beta_{el}(\dot{\theta_2} - \dot{\theta_1}) \end{aligned} \tag{2}$$

In order to prevent hyper-extension of the upper arm on the shoulder and of the lower arm on the elbow an instantaneous increase of the friction torques is added for specific ranges of q (Alg. 2).

Get θ_1,θ_2;
Calculate s_f and e_f with Eq. 2;
if $\theta_1 > 80° \vee \theta_1 < -100°$ **then**
  $s_f = 2s_f$;
end
if $(\theta_2 - \theta_1) > 150° \vee (\theta_2 - \theta_1) < -10°$ **then**
  $e_f = 2e_f$;
end

Algorithm 2: Friction evaluation algorithm

2.3 Muscles

2.3.1 Muscle models

The muscle model used is a Hill muscle model [26]. It contains a parallel spring K_{pe} simulating the passive elastic components of the muscle which is primarily produced by the connective tissues within the muscle. The series elastic component K_{se}, on the other hand, mimics the tendon stiffness. The contractile component is composed by a contractile element A producing the muscular force F_m and by the dashpot β_{pe} providing viscous friction opposed to the motion [27]. As visible in Fig. 1 the actual tension developed by the muscle F is different from the active tension developed by the contractile element F_m.

Muscle spindles are known to work in parallel with the muscle and they are modeled as springs, one for position feedback k_p and one for velocity feedback k_v [28]. Hence, the sum with its parallel produces the total stiffness and damping of the element.

$$\begin{aligned} k_{PE} &= k_{pe} + k_p \\ \beta_{PE} &= \beta_{pe} + k_v \end{aligned} \tag{3}$$

The first order differential equation relating the two quantities is the following:

$$F_m = F - k_{PE} + \frac{k_{PE}}{k_{SE}}F - \beta_{PE}(\dot{x} - \frac{\dot{F}}{k_{SE}}) \tag{4}$$

The feedback values have been computed by approximation of experimental findings. For the type II discharge, hence the position feedback values, approximation in Eq. 5 is used and for the type Ia discharge the one in Eq. 6 [11, 12].

$$\begin{aligned} II_{discharge} &= 4.3\dot{x}^{0.6} + 2x + 82 \quad for\, \Delta x > 0 \\ II_{discharge} &= 2x + 82 \quad for\, \Delta x < 0 \end{aligned} \tag{5}$$

$$\begin{aligned} Ia_{discharge} &= a\frac{\Delta x}{\Delta t} + 82 \quad with\, a = 10\, for\, \Delta x > 0 \\ Ia_{discharge} &= a\frac{\Delta x}{\Delta t} + 82 \quad with\, a = 0\, for\, \Delta x > 0 \end{aligned} \tag{6}$$

In this way both feedback signals respect experimental results in which it is proved that: 1) the type II discharge is proportional to stretching length and its maximal activity is at the length peaks and 2) the type Ia discharge is silent during release, hence during $\Delta x < 0$.
For what concerns Golgi tendon organs (GTO), located in the muscle tendon, and its type Ib afferent discharge, the model used is a multiplicative constant k_f. The deformation of the tendon is proportional to the exerted force, hence Golgi organs sense directly the force (especially if exerted by active muscle fibers rather then if transmitted by passive tissues) [14]. The equation used to model the behavior of Golgi organs is proposed here (Eq. 7) [13]:

$$Ib_{discharge} = k_f * F_m \tag{7}$$

The values for the constants used and the delay imposed to the feedback values are reported in Table 3.

2.3.2 Force optimization

In order to generate random trajectories for both training ($n_1 = 600$) and testing ($n_2 = 200$), a random torques generator has been implemented

which produces different net joint torques for both the shoulder and the elbow joint. The upper and lower boundaries for the torques are chosen in the range $[-5, +5]\,Nm$. From the torque couple $\mathbf{T} = [T_{net_1}, T_{net_2}]$ a constrained optimization routine (Sequential Least Squares Programming, SLSQP) is performed, to obtain the actual muscle force. The cost function $V(x)$ minimized is the sum of muscle forces (the actual force produced by the muscle F_m)

$$V(x) = \sum_{i}^{4}(F_{mi}) \tag{8}$$

and the search space for the force value is included in the range $[0, Fm_{maxi}]$ with $Fm_{maxi} = PCSA_i\sigma_{maxi}$. The physiological cross sectional area has been taken from [26] and the maximal tension in the muscle has been chosen as $40\frac{N}{m^2}$ for extensors and as $80\frac{N}{m^2}$ for flexors [29, 30]. The equality constraint equation can be deduced by applying Newton's laws on the free body diagram in Fig. 1 and it is provided here:

$$\begin{bmatrix} r_{1f}sin(\alpha_{1f}) & 0 \\ -r_{1e}sin(\alpha_{1e}) & 0 \\ 0 & r_{2f}sin(\alpha_{2f}) \\ 0 & -r_{2e}sin(\alpha_{2e}) \end{bmatrix}^T \begin{bmatrix} F_{1f} \\ F_{1e} \\ F_{2f} \\ F_{2e} \end{bmatrix} - \begin{bmatrix} T_{net_1} \\ T_{net_2} \end{bmatrix} = 0 \tag{9}$$

α corresponds to the angle between the working direction of the muscle and the link. It is computed for each time step by geometrical construction means using the values of r and d in Table 3. Respectively, they represent the distance from the joint, distally r and proximally d. All muscles are considered mono-articular for simplicity in the optimization process and in the calculation of the joint space state.
The real pulling force is obtained solving eq. 4 for F numerically (Backward Differentiation Formula, BDF). The force-length relationship of the muscle is

$$F(l) = 1 - \frac{(l - l_0)^2}{l_{width}^2} \tag{10}$$

with l_0 the resting length of the muscle and l_{width} the breadth of the length-tension curve [31]. With the optimized forces, the related muscle torques are computed and integration to the next step is performed.

2.4 Model architecture

A spiking neuron model, is a mathematical description of the properties of neural cells in the nervous system that generate sharp electrical potentials across their cell membrane, roughly one millisecond in duration. In order to respect biological findings the single neuron is modeled with a Leaky Integrate and Fire type (LIF) neuron, which is an adaptation of the classic Integrate and Fire (IF) neuron [32]. The adaptation w.r.t. IF is the insertion of a leaking current from the membrane

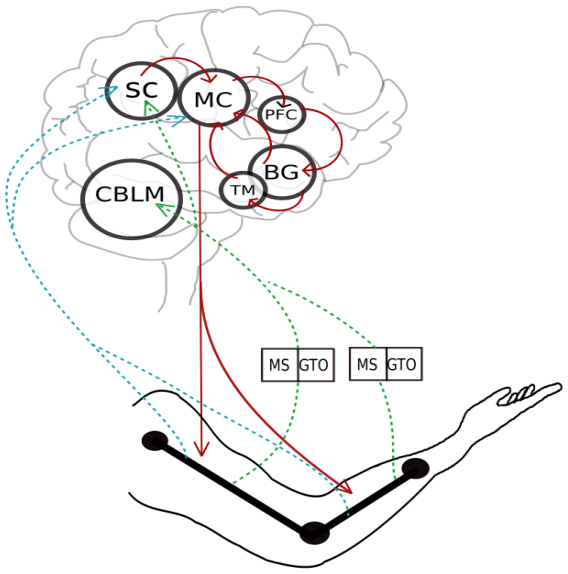

Figure 3: *Arm model, afferent (green) and efferent (red) connections to and from the involved areas. Areas: sensory cortex (SC), motor cortex (MC), prefrontal cortex (PFC), basal ganglia (BG), thalamus (TH), cerebellum (CB), muscle spindles (MS), Golgi tendon organs (GTO). In blue the path of the visual feedback back to the sensory cortex and the motor cortex.*

mimicking the diffusion of ions in non-equilibrium conditions. The membrane equation is the following:

$$I(t) = -\frac{u(t) - u_{rest}}{R_m} = C_m\frac{d(u(t) - u_{rest})}{dt}$$

with $u(t)$ the membrane potential and $R_m\,C_m$ the membrane impedance components. When the positive input $I(t)$ overcomes the threshold barrier, hence $I(t) > I_{th} = \frac{u_{th}}{R_m}$, the neuron fires a spike. All the areas in Fig. 3, but the prefrontal cortex (PFC), are modeled with Spiking Neural Networks (SNN). PFC is modeled as a fully connected neural network (ANN) since its tasks respond to more continuous input and to a more symbolic-like processing of data [20].

2.4.1 Nengo and Neural Engineering Framework

The Neural Engineering Framework (NEF) [33] is based on three fundamental principles:

- **Representation**: A neuron population represents a time-varying vector of real numbers using linear and non-linear encoding.
- **Transformation**: Linear decoders are used onto those vector to compute analytically the population connections.
- **Dynamics**: The vectors are considered as state variables in a dynamical system.

Nengo is a NEF-based neural simulator in which ensembles describe what information is being represented,

and connections describe how that information is transformed.
In this work, all the simulations are run in Nengo or in Nengo Deep Learning (Nengo-DL). The latter allows hyperparameter optimization, the use of the GPU and the insertion of TensorFlow nodes [34]. All the code is written in Python.

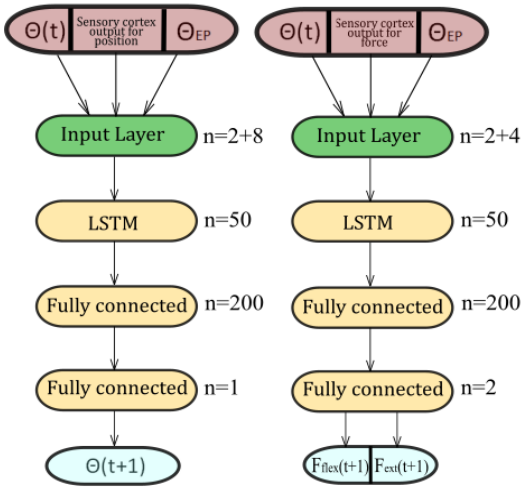

Figure 4.A Figure 4.B

Figure 4: *Figure 4.A: On the left, the motor cortex module for position prediction. Figure 4.B the motor cortex module for force prediction.*

2.4.2 Motor and sensory cortex

The MC and SC are modeled first in TensorFlow [34] and then they are converted to SNN by using the Nengo-DL Converter (Fig. 4 for MC and Fig. 5 for SC). Since there are 10 trajectories per cluster and 60 clusters in training, there will be 10 different trained sequential models both for MC and for SC. Each model will be trained on 60 trajectories, one from each cluster. The architecture used for both areas is a sequential model with the first layer being a Long-Short Term Memory (LSTM) and the subsequent layer being spiking fully connected. LSTM are a novel type of recurrent neural networks which excel in the processing of time series data, since they can cope with lags of unknown duration in the input (feedback delays and axonal delays) [35]. The standard configuration of an LSTM includes a cell, an *input gate*, an *output gate* and a *forget gate*. The cell remembers values over time intervals and the gates modulate the flow of information into and out the cell through the cells state vector.
The SC is known to create topographical maps in the brain, hence transforms the information in input into a different dimensionality [36]. Furthermore, many authors found that the encoding-decoding process resembles a frequency decomposition-like process [37, 38, 39]. Hence, the sensory cortex is trained to perform a Hilbert-Huang transform (HHT) of the feedback signals. The HHT is an algorithm which is the result of the

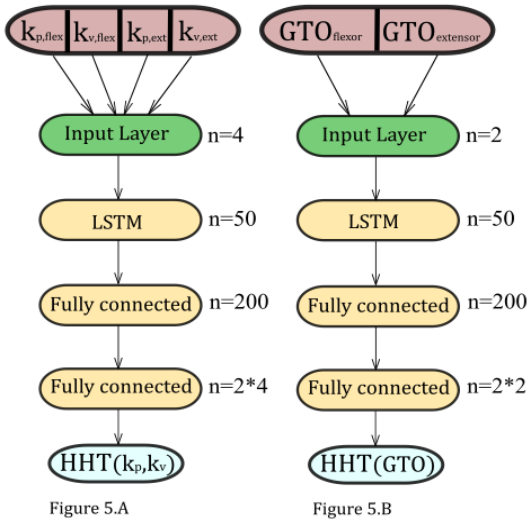

Figure 5.A Figure 5.B

Figure 5: *Figure 5.A: On the left, the sensory cortex module for position prediction. Figure 5.B the sensory cortex module for force prediction.*

empirical mode decomposition (EMD) and the Hilbert spectral analysis (HSA). EMD is used to obtain the so-called *intrinsic mode functions* (IMF) and from those, HSA is applied to obtain instantaneous frequency data. For the extraction of IMFs (iterative sifting process), a stoppage criteria is used based on two thresholds. The evaluation function used corresponds to $\sigma(t) = |\frac{r(t)}{a(t)}|$ with $r(t)$ the residual of the decomposed function and $a(t) = \frac{(e_{max}(t) - e_{min}(t)}{2}$. $e(t)$ is the envelope trajectory of the interpolation between minima and maxima of the signal $x(t)$. The sifting is iterated until $\sigma(t) < 0.05$ for a fraction $f(t)$ of the total duration of the signal ($f(t) = 1 - \alpha$) with $\alpha = 0.05$) and until $\sigma(t) < 0.5$ for the remaining fraction [40, 41].
Respectively, as visible in Fig. 5, the position modules of SC are trained to predict the HHT of the position and velocity feedback while the force modules are trained to predict the HHT of the GTO feedback. Those values are then provided to the MC as input together with the position visual feedback value [42]. MC modules (Fig. 4) have the same structure of its SC companions. Respectively the position modules predict $\theta_{1,2}(t+1)$ and the force modules $F_{flex,ext}(t+1)$.

2.4.3 Prefrontal cortex - basal ganglia - thalamus

It has often been argued that, beside systematic responses to known inputs, the human is capable to respond in a flexible manner to new inputs or to new context. This flexibility is supposed to rely on symbolic processing, that is the capability of our brain to represent information in the form of abstract variables [20]. In this matter, the variable-binding mechanism of the PFC-BG connection, shows through the use of indirection (similar to a pointer in computer science), that the processing of novel stimuli can be supported

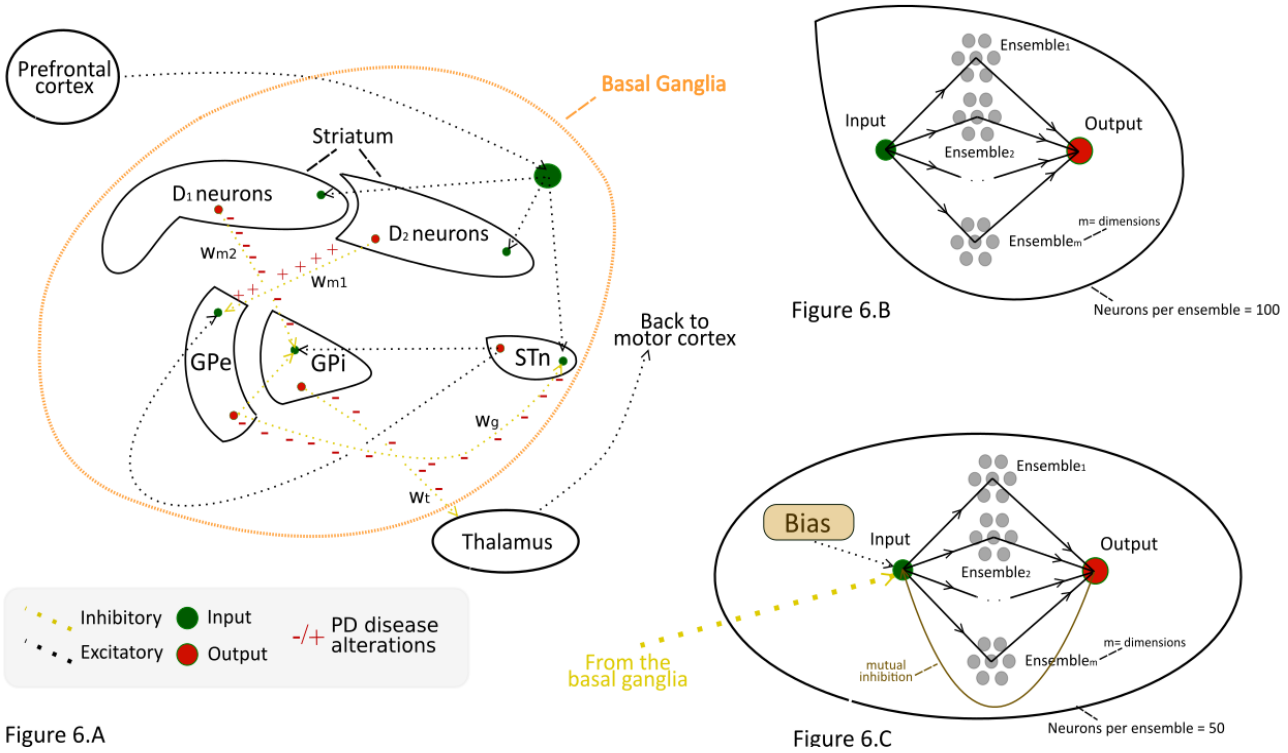

Figure 6: *Fig 6.A: Model of prefrontal cortex, basal ganglia and thalamus. $+/-$ indicate PD model alterations. Fig. 6.B Inside of each of the areas in the basal ganglia. It is composed by an input node, an array of ensembles and an output node. In the output node, the connection with the subsequent area has a different parameter-dependent function for each area, according to its behavior (inhibitory or excitatory). Fig. 6.C: Inside of the thalamus. Input node, output node, array of ensembles and mutual inhibition connections (needed since dimension mutually inhibit each other). In order to suppress low responses and strengthen high responses, a constant bias is added to each dimension (trajectory in a cluster).*

by those means.

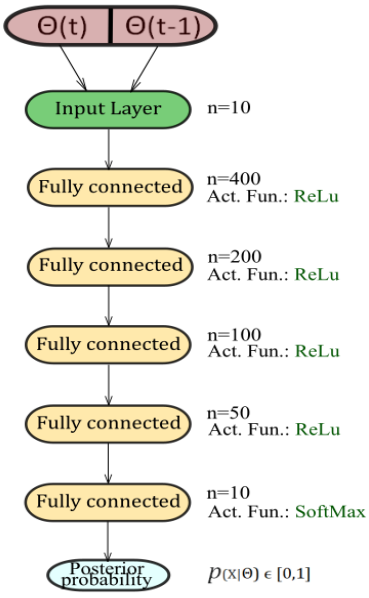

Figure 7: *Pre-frontal cortex model architecture.*

It is shown that dopamine neurons code reinforcement *prediction errors* [44, 45], which is a fundamental signal in many reinforcement learning models. This view, shows how the BG fits well the action selection task which it is entitled for, suppressing competing actions and facilitating the most appropriate one [46], hence providing flexibility in the responses to novel inputs. When looking at the velocity profiles of reaching point movements[47], writing trajectories [48] or vestibular control process, it is noticed how the brain seems to first constructs an abstract representation of the movement, (encoded as a sequence of boundary conditions) then converts those conditions into the actual trajectory by using laws that constrain movement (minimum jerk, point of equilibrium and so on) [49]. For this reason, in our model, the PFC is an artificial neural network which computes a score proportional the amount of '*jerk minimization*' for each of the trajectories in a receptive field (cluster), which is then conveyed to the BG. The prefrontal cortex output score is forced in the range $[0-1]$. This is possible after the insertion of a *softmax* type activation function [50] in the last layer, while each previous layer uses a Rectified Linear Unit (ReLu) activation function. The former forces the output distribution in a probability-like range by compressing a k-dimensional vector z in a k-dimensional vector $\sigma(z)$ in a range $[0-1]$, while the latter is defined as the positive part of its argument, hence $f(x) = x^+ = max(0, x)$. Furthermore ReLu activations functions are scale in-

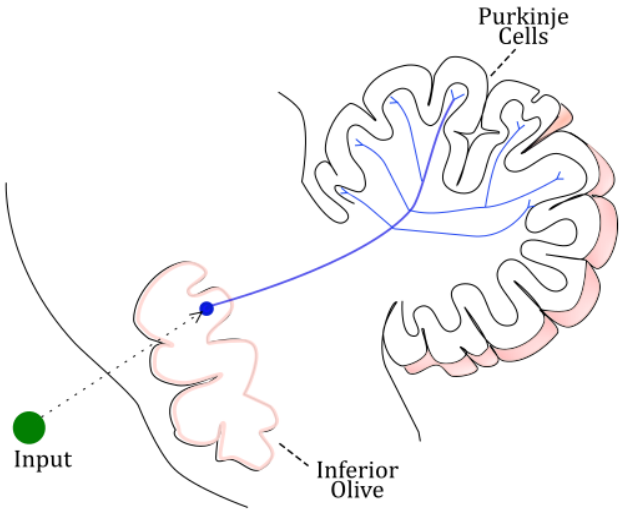

Figure 8.A

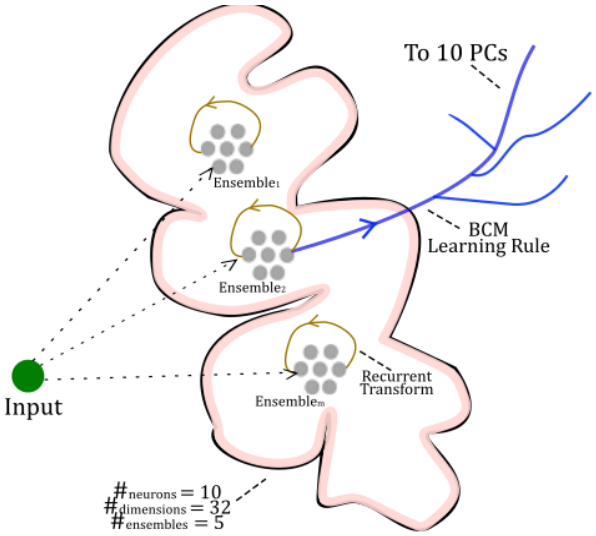

Figure 8.B

Figure 8: *Fig 8.A: Inferior Olive (IO) and Purkinje Cells model. In blue the climbing fiber connections to make synapse with the PCs. In green the input node conveying all types of feedback used in the whole model. Fig. 8.B Inside of the IO. An array of ensembles is used with ratio* $\frac{IO\,neurons}{Purkinje\,cells} = 10$. *The learning rule in the synaptic connection is the Bienenstock–Cooper–Munro (BCM) rule [43]. The recurrent transform is used to link each neuron in the ensemble to mimic weakly coupled oscillators.*

variant and computationally efficient, which makes them perfect for large scale modeling [50].
The basal ganglia performs an action selection task in a reinforcement learning manner. The thalamic input will be the choice made by the BG and the thalamic output will be an amplification of the correct choice and inhibition of the wrong ones (Fig. 6). Those two structures are adapted from the work of T. Stewart and C. Eliasmith [21, 51, 52, 16]. In our model, the signal coming from PFC is first processed by the striatum and the STN. In this moment, the substantia nigra pars compacta (SNc) excites the striatum through the D1 dopamine receptors while inhibits it through D2 dopamine receptors. The activation of D1 receptors in the striatum (selection pathway) stimulates the striatum itself to inhibit the GPi which is the actual output of the BG. Since the GPi inhibits the thalamus, the actual signal for the selected action will be close the zero, dis-inhibiting the neurons associated with that action. Important parameters of the model are l_g and l_e which adjust the degree of tonic dopamine in the D1, D2 modulated pathways. In order to do so the transform of the input node-striatal connection is of the form

$$tr_{input-striatum} = \begin{cases} \mathrm{w}_s * (1 + l_g) & \text{for D1 pathways} \\ \mathrm{w}_s * (1 - l_e) & \text{for D2 pathways} \end{cases}$$

with $w_s = 1$ the input node synaptic weight.
The w_t parameter adjusts the afferent synaptic strength to the STN, hence decreasing it results in less inhibition in the thalamus. SNr and GPi are both included in the GPi and the internal split can be modified by varying the parameter w_p. The variation of w_p in the range $[0 - 0.9]$ affects conditionally the activity of GPi/SNr leading to different activity levels of STN/GPi. w_{m1} and w_{m2} represent the connection weights of the inhibitory connections D1 to GPe and D2 to GPi, while w_e and w_g the connection weights of the GPe with the GPi and the STN. All parameters have been taken from [51, 53] for the healthy subject. w_{m1} and w_{m1} in the initial model shared a common variable, but PD induces different behavior in the striatal connection to the GPe compared to the GPi, hence a split in two different parameters was implemented.
The thalamus is intended to work in tandem with the BG network. It converts the output of the basal ganglia into a signal with approximately 1 for the selected action and 0 elsewhere, hence beside its recurrent internal connection it does not have further dynamics.

2.4.4 Cerebellum

Given the high computational complexity of the model and given the relevance of the cerebellum into tremor generation being low the cerebellar modeling is approximated to the core. Surely, it covers a role into modulating tremor as if it was an intentional movement [54, 55] but most likely it is not the central pattern generator (CPG) of the tremor itself.
The cerebellar model is *slaved* to the rest of the model. With *slaved* it is intended that only inputs are provided to the CBLM and its feedback, hence its modulatory compensatory behavior, is not fed back neither to upper brain centers nor to the descending motor pathways. The architecture (Fig. 8) is composed by the inferior

olive nucleus (IO) and by a spiking perceptron composing the Purkinje Cells layer and it is modeled directly in Nengo. The inferior olive is composed by $n = 5$ weakly coupled oscillators with each of them having 5 neurons and 18 dimensions each. Each neural ensemble possesses a recurrent transform r_t such that it becomes an ensemble of coupled oscillators. A oscillator can be implemented with a neural ensemble with the following dynamics:

$$\dot{x} = \begin{bmatrix} 0 & -\omega \\ \omega & 0 \end{bmatrix} x$$

with $f_{osc} = \frac{\omega}{2\pi}$. According to the NEF principle, to implement a specific dynamic this equation must be converted into a feedback function, hence

$$\dot{x} = f(x) \Rightarrow f_{feedback}(x) = x + \tau f(x)$$

$$f_{feedback}(x) = x + \tau \begin{bmatrix} 0 & -\omega \\ \omega & 0 \end{bmatrix} x = \begin{bmatrix} x_0 - \tau\omega x_1 \\ \vdots \\ x_{17} + \tau\omega x_{18} \end{bmatrix}$$

The feedback function or recurrent transform takes the IO output and provides it back to the input, along with the input itself which is a vector containing all the feedback signals in a direct (from the spindles, GTO, visual feedback) or in an indirect (from the SC) form. The output of each ensemble is conveyed to 10 Purkinje Cells and the connection weights are updated using the BCM rule [43].

2.5 Offline Training

The only trained areas are the SC, MC and PFC. They are trained respectively to compute the HHT (sensory cortex), predict position and force (motor cortex) and compute a jerk-minimization related score (prefrontal cortex). To the ten different modules of SC, one trajectory per cluster is provided to the each module, with the targets being the HHT of the feedback values computed analytically. Then the output is delayed according to delays interval of muscle spindles and Golgi organs and attached to the position $\theta(t)$ and to the endpoint position θ_{EP}. This will be the input of the MC together with the endpoint position and the target position prediction $\theta(t - \Delta_{vis})$ with Δ_{vis} the visual feedback delay. For all the clusters and all the trajectories per cluster, jerk is computed and provided to the PFC as input. The target is a vector with positive class corresponding to the index of minimum jerk and zero elsewhere. The basal ganglia and thalamus are untrained dynamical models which mimic the dynamicist function hypothesized from experiments in the human. Same holds for the cerebellum.

2.6 Parkinson disease model

In order to mimic PD, the healthy model connectivity weights and dopamine levels have been altered. Parkinson was induced by changes in the basal ganglia and its connection with the thalamus, so for both the healthy and the PD case all the other areas remain unchanged. Wichmann and De Long [56] show how in PD conditions the D2 striatum-GPe connection strength increases while the D1 striatum-GPi connections weakens. The values for $w_{m1} = 14$ and $w_{m2} = 10$ are chosen by minimizing deviations w.r.t experimental findings in [57, 56, 58]. Furthermore, the GPe-STN connection weakens during PD, hence its weight w_g it is lowered from 1 to 0.9.
It has been known for decades that the output of the BG, mainly the GPi, is hyperactive in PD [59, 18]. The Gamma amino-butyric acid (GABA) inhibitory projections towards the thalamus are massive, and they induce a reduction of thalamo–cortical activity in PD patients ([59]). The GPi-thalamic connection weight w_t increase in PD patients ([56, 60]) will be mimicked setting $w_t = -2$.
In order to investigate dopamine depletion effects, the values of l_e and l_g are varied one at the time among $l_e = l_g = 0$ and 1 with a step of 0.2, hence a 6×2 sensitivity analysis of the model is carried out. The non-changing value is set $l_{e,g} = 0.2$ with 0 no dopamine at all, in order to investigate the interaction of the response of two different possible sources of abnormal BG activity (D1 and D2).

3 Results

3.1 2-link model

In Fig. 9 the bio-mechanical validity of the 2-link model and of the feedback functions is tested along with the correlation among the state variables (Suppl. Fig. 5.1).
In these plots the variables are presented as continuous rate values, but when transmitted in the networks they take the form of spikes. Type II discharge is silent when the muscle length is smaller than l_0, grows along with length and partly with elongation and has maximal value when the length is maximal. Type Ia discharge, is clearly proportional to lengthening velocity and is silent during release. Golgi feedback and the force trivially match in behavior, and both the angle and the force respect what it is seen graphically in the attached simulation. As expected position feedback correlated well with all the other variables. The clear ones are velocity feedback and lengthening $\rho = 0.96$, $P < 0.01$, position feedback and length $\rho = 1$, $P < 0.01$ which correctly coincides inversely with the position feedback and muscular angle correlation $\rho = -1$, $P < 0.01$. Good correlation between the muscular angle and all kinds of feedback is found. Furthermore, when

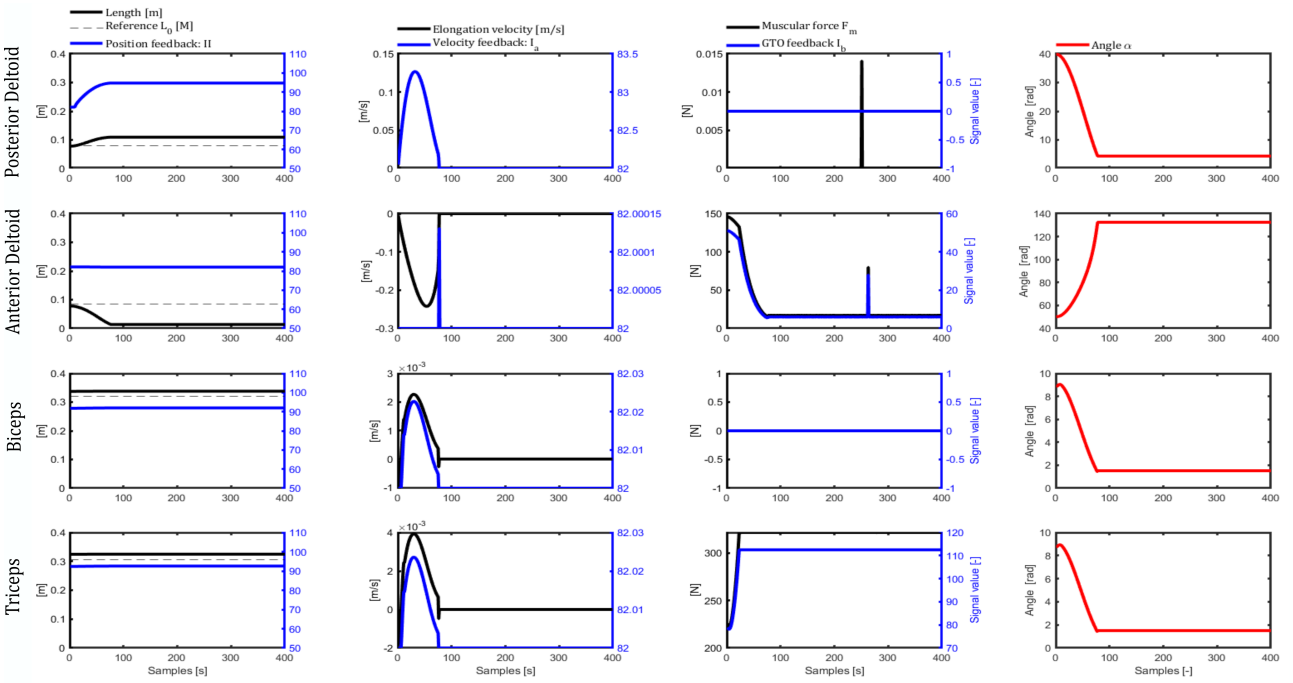

Figure 9: *State and feedback variables with* $T = [-4.52, -1.65]\ Nm$

looking at the correlations of length, elongation and angle a typical muscular behavior is found. Increasing the muscle length often coincides with decreasing lengthening velocity, since the object has been reached ($\rho = -0.59,\ P < 0.01$). Same holds for the angle between the muscle and the distal attachment point, which must decrease in order for the muscle to lengthen ($\rho = -1,\ P < 0.01$).

3.2 Single areas testing

In order to evaluate each of the areas performance, the areas are tested sequentially. The order of presentation of the results respects, the open-loop flow of the simulation.
The trained areas of the model (SC, MC, PFC), showed an excellent capability in predicting time series as position and force.

The sensory cortex prediction of position HHT ($MAE < 10^{-4} \pm 5 * 10^{-6}$) and of force HHT ($MAE < 10^{-3} \pm 2 * 10^{-5}$) are almost ideal. The prediction of the next position θ_{t+1} by the motor cortex ($MAE = 0.04 \pm 0.04$) accurately follows the targets (Fig. 11). Same holds for forces prediction ($MAE = 4.88 \pm 17.86$), if not for an high standard deviation of the error. This unusual STD is due to the discrete latency forced onto the LSTM cells to respect feedback delay and to the clustering process. Mainly, this behaviour is found to happen at the trajectory transition times and in clusters with slightly different trajectories.
The prefrontal cortex had the aim of assessing a jerk-related score when provided with kinematics data.

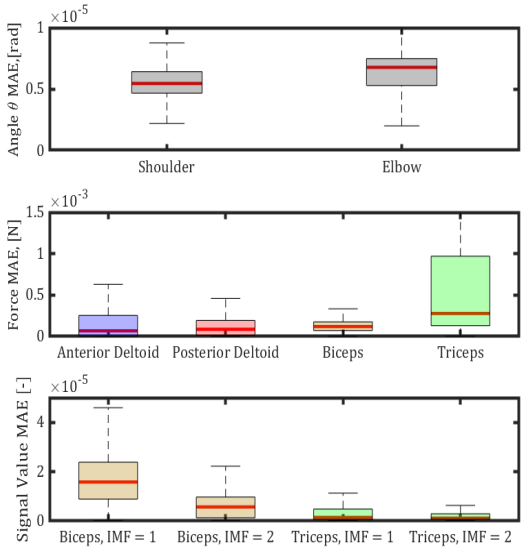

Figure 10: ***Top****: AE of joint angles prediction.* ***Middle****: AE of muscular forces.* ***Bottom****: AE of sensory cortex modules for force decomposition.* ***All****: All values are calculated averaging among the absolute error (AE) of each of the ten related cortical modules.*

Each m_{th} class is related to the respective motor cortex position modulus which provide the m_{th} input. A class having the highest score implies that the predictions of the corresponding modulus are associated by the PFC to the ones producing minimum jerk. In the learning curve (Fig. 12) it is shown how, coherently with the motor cortex elbow synergy having an higher error than its shoulder companion, the cross-entropy loss of

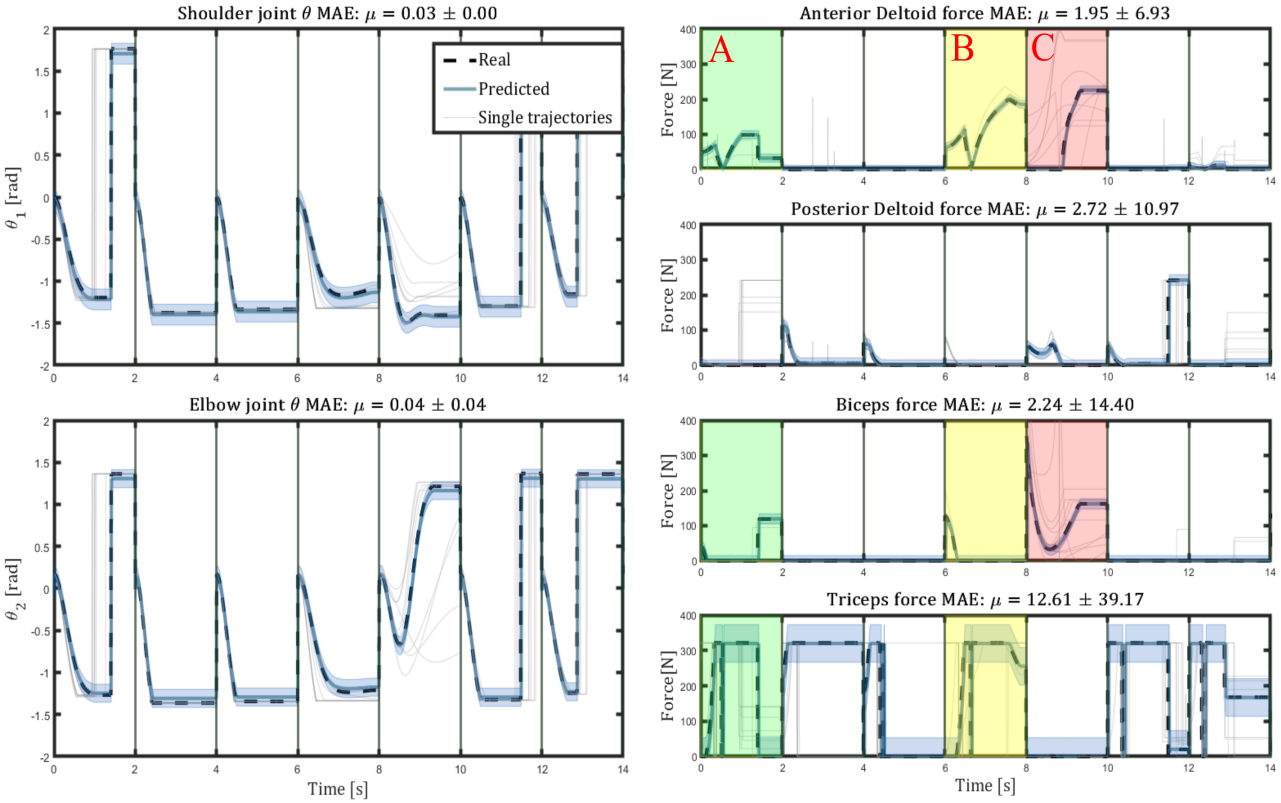

Figure 11: *Real v.s. predicted angle (left) and real v.s. predicted force (right). With shaded green, yellow and red three trajectories in which co-contraction happens and in shaded blue the standard deviation of the absolute error (AE). It is visible how the prediction follows the expected values.*

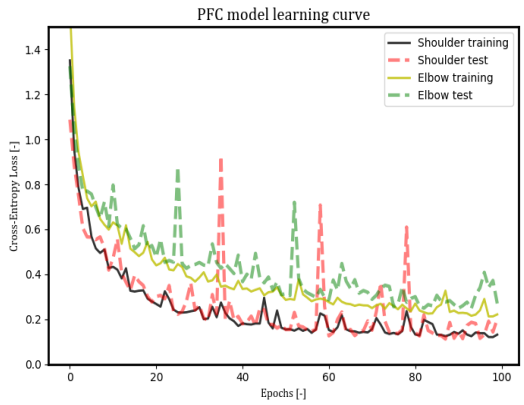

Figure 12: *PFC learning curve. At $n_{epochs} = 50$ the elbow PFC shows overfitting.*

the PFC is higher for the elbow. To avoid overfitting behavior, as in the elbow synergy after $n_{epochs} = 50$, the shoulder synergy was trained for $n_{epochs} = 80$, while the elbow synergy for $n_{epochs} = 50$.
In the iterative clustering algorithm the first trajectories inserted in the cluster are the ones with minimal MSE w.r.t the cluster centroid. This way of creating clusters created an imbalanced classification problem which together with the high number of output labels (10) and the higher complexity of multi-label classification problems [61] called for a resampling of the train set. A combined over-sampling and under-sampling approach called Synthetic Minority Over-Sampling Technique (SMOTE, [62]) was adopted. SMOTE first selects a minority class instance and its k nearest neighbors, then synthetic instances are generated as convex combination (on a straight line) every two neighbors of the minority class considered. The resampling process reached an accuracy of $84 \pm 29\%$ for the shoulder and of $82 \pm 37\%$ for the elbow module.

For what concerns the basal ganglia-thalamic circuit, in the healthy cases the mean spiking frequency rate (MSFR) of all the four areas match experimental findings [63, 64, 57]. Same holds for the PD model areas which have been tuned to reproduce previous findings ($MSFR_{STN} = 42.08\,Hz$, $MSFR_{GPi} = 80.9\,Hz$, $MSFR_{Th} = 24.4\,Hz$ [58, 63]).
The firing patterns both in the healthy and in the Parkinsonian case, are consistent with experimental findings ([56]). Specifically, the STN spiking pattern is sparser in the healthy case while it is more self-sustained in the PD. Its baseline rises from 12.97 to $41.25\,Hz$ and the pattern becomes more dependent on input variations as in [65]. In the middle two columns of Suppl. Fig. 5.2, the MFSR does not seem the mean of the local field potential in figure. The difference originates in the fact that is plotted only one of the ten ensembles of each area and the average is done in all the ensemble to give

the reader the idea of the 'whole-area' dynamics.
Clear is the increase of synchrony in the pallidal oscillations, both in neurons of the internal and the external globuli [56, 66]. Furthermore, a stronger bursting behavior is found in both the GPe and the GPi as in [67] (Fig. 13). This can be seen from how all the neurons from the same ensemble contribute to the same pattern toward the MSFR (PD) while in the healthy case, the neurons across the ensembles are more desynchronized.
The thalamus itself shows a decrease in the fire rate baseline (35.45% from $37.64\,Hz$), in oscillatory activity (mean spectral power) [60] and an increase in bursting behavior ($MFSR = 54.69 \pm 5.50$) as in [60, 18, 68, 58] consequent to the increased spike rate of the GPi, the BG inhibitory output to the thalamus. Furthermore, the thalamus presents an increase in the oscillation power in the tremor band ($\sim 300\%$) and a very strong decrease in γ oscillations ($\sim 54.8\%$).
It has been found that the in general the MSFR of each of the basal ganglia areas is sensitive to co-contraction and has its maximal peak (GPi, GPe) or valley (STN, Th) in a slightly delayed position w.r.t. to the start of the co-contraction (compare trajectories A,B,C in Fig. 11 and Suppl. Fig. 5.2). This behavior is found to happen for all the ensembles and all the clustered trajectories tested. We chose one ensemble where the STN is excessively spiking. This allows the investigation of the aforementioned coherency phenomena without detrending the MSFR. In panel A (Suppl. Fig. 5.3), where all the clusters are merged together and re-sampled with a bin size of $250\,ms$, it is shown how the STN and the TH correlate negatively with the elbow angle and the bicep force respectively in the healthy case and in the PD one. Furthermore comparing healthy and PD thalamic-STN MSFR shows an inverted correlation ($\rho = 0.13,\ healthy$ and $\rho = -0.35,\ PD$) and weaker in the healthy case. The mutual correlation of force and position is equal in both cases, since the body model is left unchanged.
In panel B, one mean value per each cluster is taken to represent the regressed variables. This allowed torques to be dimensionally consistent with the remaining variables. Again, the STN and the thalamus negative correlation with elbow position and biceps force behave as in the similar case of panel A. Furthermore, the STN - shoulder torque correlation ($\rho = -0.588,\ p = 0.035$ is lost in the PD case. When investigating the tremor band behavior across neural areas, it was noted that, in the basal ganglia it correlates positively ($\rho > 0.6,\ p < 0.05$) with the bicep force, both in healthy and in PD. On the other hand, a strong thalamic - bicep force correlation ($\rho = 0.75,\ p < 0.001$) appears only in the parkinsonian case. Beyond this, it is noted an overall increase of correlation between tremor frequency thalamic oscillations and the tremor power in the three BG areas. In the healthy case, the $PSD_{Thal,4-8Hz}$ correlates positively with the MAE of the position prediction, but this disappears completely in the right column. Furthermore, as the shoulder torque increases the GPi tremor PSD component increases ($\rho = 0.626,\ p < 0.05$), phenomena that does not happen in the healthy case. In the PD case, the GPe-GPi tremor power correlation lowers while the GPe-STN becomes higher. However, it should be noted that all the Spearman's ρ in panel C are positive.
Panel D (Suppl. Fig. 5.3) shows the correlations of the tremor component of each area while l_g or l_e are varied in turn in the range $[0-1]$ with a step of 0.2. It was found that, only in the healthy case, the amount of tremor oscillations in the GPe grow together with Striatal D1 neurons activity. Furthermore no correlation were found between D2 dopamine variation and tremor power in any BG-TH area. In the parkinsonian case, the correlations between GPi, GPe and STN tremor power while l_g varies, and are much more evident then in the healthy case which only presents correlations for the GPi-STN combination.
Moving on to the cerebellum, neither the inferior olive neurons nor the Purkinje cells show any significant changes between parkinsonian and healthy case, coherent with the fact that no changes are done to its structure, but only slightly to its inputs. The only significant change is in the γ and in β band power which respectively increase and decrease in the Parkinson model. The MSFR of the inferior olive and the Purkinje cells are slightly higher than experimental findings [69, 70, 71]. The IO MSFR (2.83 ± 1.83, healthy) is found to be an average between very different neurons, some spiking up to $40 - 80Hz$ and some spiking at a very low frequency ($0 - 1.5Hz$). Inappreciable changes in neuronal MSFR proportions were found in the PD case besides for an increase in the simple spike power. A priori of its changes with PD, the IO presents a typical oscillatory behavior, which grows toward the end of the trajectory. It was found that IO spiking rate is not affected by changes among the kinematic-dynamic variables of the trajectories when a long-time average is taken into consideration. One can see this, in the existence of no similarity between the IO MSFR periodicity across trajectories, and the state variables in Fig. 11. This is confirmed numerically, by the non-significant correlation between the olive MSFR and θ_{elbow}, F_{Biceps} and $F_{Triceps}$ (Suppl. Fig. 5.3, panel B). While evaluating power in the tremor band (panel C) of the healthy model, both the IO and the PCs show clear positive correlations ($p < 0.01$) with the MAE and the STD of the predicted trajectory, hence with mechanical tremor. In the PD model, on the other hand, no correlations are found.

4 Discussions

Data from experiments in MPTP monkeys as well as from recordings in PD patients suggest an abnormal synchronization of neural activity in the whole cerebral oscillatory network [67]. Medications used to decrease

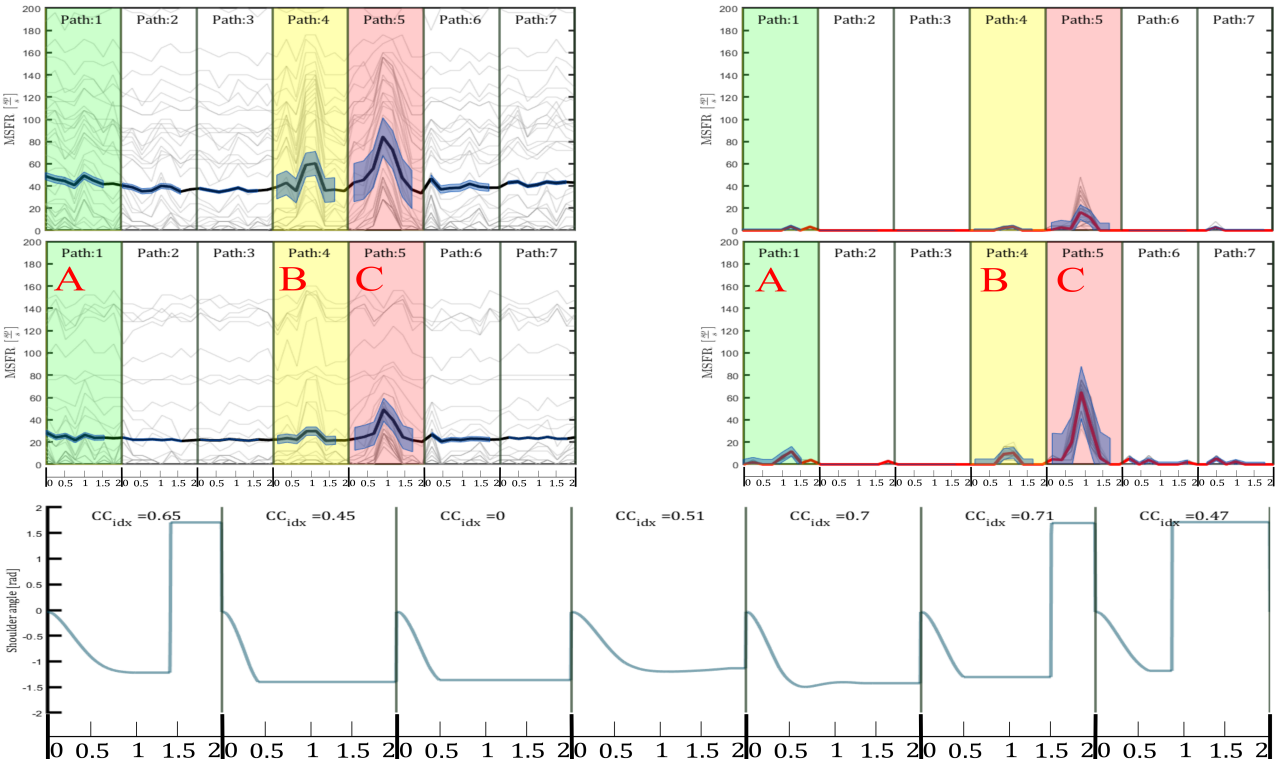

Figure 13: *MSFR of GPe (top) and of GPi (middle) for seven clustered trajectories. Clear synchronization is seen among pallidal neurons. The co-contraction index is calculated using* $CC_{idx} = \frac{\sum F - min(\sum F)}{max(\sum F}$ *and its clearly higher in trajectories A, B, C where the bursting behavior is maximal. No similarity or correlation is found with the 2D span of the trajectory (shoulder angle in bottom plot).*

involuntary antagonistic muscle contraction (primidone,propranolol, beta-blockers) can reduce resting tremor but they have withdrawal and side effects (e.g. addiction) [72, 73]. Moreover, tremor is an independent symptom, it does not progress at the same rate of the bradykinesia, rigidity or gait [74] and it can occur contralaterally to the most affected side (bradykinesia, rigidity are most prominent, [75]). The aforementioned reasons, combined with absence of clear correlations between the main PD physiological symptom (striatal DA-D) and tremor amplitude/onset, shows us the importance of understanding the underlying biophysical reasons behind tremor generation.

Evidence suggests that the BG (*finger*) induces PD tremor via excessive inhibition to the thalamus (*switch*) and abnormal firing patterns, which in turn generate rhythmic bursting activity in the related thalamic cells [18]. Furthermore, the thalamus is shown to generate stronger bursting behavior and lower mean spiking rate, hence facilitating the generation of tremor frequency oscillations [67, 76, 18]. The *finger-switch-dimmer* theory adds to this equation the cerebellum (*dimmer*), which maintains its known properties, and considers PD tremor as it would a voluntary movement, hence modulating its properties. As already mentioned, in PD conditions the D2 striatum-GPe connection strength increases while the D1 striatum-GPi weakens [56]. Furthermore, it is shown how the GPe-GPi connection strength is increased.

In our PD model, the GPe MSFR decreases, given the higher inhibition of D2 neurons, hence the GPi is inhibited less. We show how the STN, with its increased firing rate, contributes to the excitation of the GPi itself. The GPi increased MSFR inhibits the thalamus, which modifies its oscillatory behavior into an almost fully bursting behavior, this allows for the emergence of tremor band power. In our model the thalamus is the only area which presents a clear increase of PSD in the tremor band ($+8.17\%$), confirming surgical findings asserting that the best brain stimulation area is the ventro-lateral posterior thalamus. [77, 76]. It is highlighted how an increase of dopamine (either via D1 or D2 neurons) does not resets the thalamic spectral component in the tremor band in a Parkinsonian patient further confirming the insufficiency of levodopa treatments. Furthermore, the loss of the correlation between thalamic tremor power and MAE of the predicted trajectory in PD conditions is coherent with the introduction of a new source of tremor (Parkinson) compared to the healthy case where the only tremor felt were the oscillations in the trajectory prediction.

We propose that the GPe-GPi activity, which is known to receive a modulatory effect from pallidal dopamine, in concert with the more direct GABAergic inhibitory and glutamatergic excitatory actions of the striatum [78], enhanced from the increased activity of its inner feedback loop , creates a favorable environment for the generation of thalamic tremor oscillations via excessive

inhibition of the thalamus. Only proprioception and not tremor seemed capable of taking advantage of the redundant networks in the brain after ventrolateral (VL) thalamotomy and allow for voluntary movements [79]. This, the thalamic high sensibility to oscillations [80] and the power in the tremor band being higher only in the thalamus among the four areas of the BG-TH loop, suggests us that the thalamus (*switch*) is the PD tremor central pattern generator. The excessive inhibition of the basal ganglia (*finger*), induces changes in thalamic activity. However, our result show how it is the GPe-GPi connection that synchronizes tightly and that initiates the typical basal ganglia bursting behavior. Surgical findings [6, 81] show how STN deep-brain stimulation (DBS) tends to increase GPi firing rate, converse to expectations. At the same time, the firing pattern becomes more regular with a significant reduction in burst rate [81, 3]. Sub-thalamic DBS still alleviates tremor, reducing the excitatory push to the pallidum, but it does not either resolve tremor or restores firing rates of the pallido-thalamic connection. This confirms the hypothesis in which the GPe inhibitory levels to the the GPi cannot be restored by reducing the excitatory sub-thalamic drive. Hence, we suggest that the *finger* (BG) can only be truly lifted from the *switch* (TH) if the GPe-GPi inhibition is restored to healthy rates and levodopa-like treatments are provided to reset striatal D1 and D2 dopamine levels.
Furthermore, we found that the increased GPe-GPi activity is strongly enhanced during muscular isometric co-contraction. Given the experimental decision of using inverse dynamics optimization with constant torques, when the joint limit angle are reached, both the muscular stiffness and the force increase asymptotically as if the patient reached the object and it is holding onto it. The weight of the object could be translated into the asymptotic limit that the force increases to. This shows, how the tremor pattern generation is similar for re-emergent tremor and rest tremor, but much stronger during co-contraction. One can see in Fig. 13, how the GPi-GPe MSFR possess small peaks even in the healthy case during co-contraction. This result suggest that the basal ganglia, in particular the GPe-GPi inner loop responds to mechanical tremor in a consistent manner, a priori of the condition which caused it. This finding is confirmed by Hurtado et al. [7], which shows precise synchronization between GPi-EMG peaks for low forces, but for higher forces the GPi MSFR lowers and the synchronization becomes transient. The correlations of the BG with the force remain almost unchanged in the health and PD case, but biceps force and thalamic tremor band power correlate only in the the PD case (Suppl. Fig. 5.3, panel C). This shows how oscillations in the tremor band do not appear in the pallidus or in the striatum but in the thalamus and confirms the hypothesis of a consistent (PD or healthy) spectral response of the BG in the tremor band.
For what concerns the cerebellum, we can claim that the only plausible result is the periodicity of the IO spiking rate [82, 83] and the fact that, the periodicity of the averaged MSFR over long bins ($250\,ms$) is not affected by Parkinsonian conditions. This confirms previous findings where the average olivary activity was shown to be independent from the amplitude and from the duration of the provided input [83].

5 Conclusions and Further Outlook

We propose a model in which the combination of basal ganglia and the cerebello-thalamic-cortical loops give origin to the parkinsonian tremor. By simulating a large-scale brain network, we presented evidence of increased synchrony between neurons and increased bursting behavior in the pallidum. Consequently, increased power at the tremor frequency in the thalamus was found. Furthermore, we showed how dopamine injections neither decrease the tremor power in the BG-TH nor restore the pallido-thalamic firing rates. These results, combined with DBS on the STN regularizing only bursting pattern and not MSFR, but alleviating tremor, brings us to suggest that the GPe-GPi inhibitory connection and its weakening via pallidal dopamine depletion is the starting cause of PD tremor. This would split Helmich *finger* in two, the actual *finger* pressing on the switch being the GPi and the *hand* behind the finger being the GPe.

Amongst the limitations of our model we discuss two: 1) the *dimmer* effect is not modulated since the cerebellum model does not close the cerebro-cerebellar cortical loop and 2) only open-loop simulation. At the same time, the assumptions taken do not harm the quantitative outcomes. As with other proposed models in literature, this represents a working model on which future experiments and results may be laid, in order to either support or disprove it. Future work could focus on increasing the details and the number of the modeled areas or on comparing the model parameter space to specific experimental conditions in a closed-loop fashion. This could provide chances of understanding on a finer scale how one can intervene onto the interactions in the cortico-thalamic loop to reduce tremor in PD patients in a non-invasive manner.

Bibliography

[1] Joseph Jankovic, Kenneth S Schwartz, and William Ondo. “Re-emergent tremor of Parkinson ’ s disease”. In: (1999), pp. 646–650.

[2] Rick C. Helmich et al. “Pallidal dysfunction drives a cerebellothalamic circuit into Parkinson tremor”. In: *Annals of Neurology* 69.2 (2011), pp. 269–281. ISSN: 03645134. DOI: 10.1002/ana.22361.

[3] Christian Duval et al. “A brain network model explaining tremor in Parkinson’s disease”. In: *Neurobiology of Disease* 85 (2016), pp. 49–59. ISSN: 1095953X. DOI: 10.1016/j.nbd.2015.10.009.

[4] J. Gross et al. “The neural basis of intermittent motor control in humans”. In: *Proceedings of the National Academy of Sciences of the United States of America* 99.4 (2002), pp. 2299–2302. ISSN: 00278424. DOI: 10.1073/pnas.032682099.

[5] Henning Boecker et al. “GABAergic dysfunction in essential tremor: An11C-flumazenil PET study”. In: *Journal of Nuclear Medicine* 51.7 (2010), pp. 1030–1035. ISSN: 01615505. DOI: 10.2967/jnumed.109.074120.

[6] R. Levy et al. “High-frequency synchronization of neuronal activity in the subthalamic nucleus of Parkinsonian patients with limb tremor”. In: *Journal of Neuroscience* 20.20 (2000), pp. 7766–7775. ISSN: 02706474. DOI: 10.1523/jneurosci.20-20-07766.2000.

[7] J M Hurtado et al. “Dynamics of tremor-related oscillations in the human globus pallidus: A single case study”. In: *Proceedings of the National Academy of Sciences of the United States of America* 96.4 (1999), pp. 1–6. URL: papers2://publication/uuid/682A24CF-0E38-4A59-95B0-7637D78F69B8.

[8] Andres M Lozano and Anthony E Lang. “Effect of GPi pallidotomy on motor function in Parkinson’s disease Summary”. In: *The lancet* 346 (1995), pp. 1383–1386.

[9] P. Krack et al. “Stimulation of subthalamic nucleus alleviates tremor in Parkinson’s disease”. In: *Lancet* 350.9092 (1997), p. 1675. ISSN: 01406736. DOI: 10.1016/S0140-6736(97)24049-3.

[10] Masako Kinoshita et al. “How does voluntary movement stop resting tremor?” In: *Clinical Neurophysiology* 121.6 (2010), pp. 983–985. ISSN: 13882457. DOI: 10.1016/j.clinph.2010.01.016.

[11] Arthur Prochazka and Monica Gorassini. “Models of ensemble firing of muscle spindle afferents recorded during normal locomotion in cats”. In: *Journal of Physiology* 507.1 (1998), pp. 277–291. ISSN: 00223751. DOI: 10.1111/j.1469-7793.1998.277bu.x.

[12] S. E. Grill and M. Hallett. “Velocity sensitivity of human muscle spindle afferents and slowly adapting type II cutaneous mechanoreceptors.” In: *The Journal of Physiology* 489.2 (1995), pp. 593–602. ISSN: 14697793. DOI: 10.1113/jphysiol.1995.sp021075.

[13] Winfred Mugge et al. “A rigorous model of reflex function indicates that position and force feedback are flexibly tuned to position and force tasks”. In: *Experimental Brain Research* 200.3-4 (2010), pp. 325–340. ISSN: 00144819. DOI: 10.1007/s00221-009-1985-0.

[14] B. Koopman Van Der Kooij, H. and Frans C.T. Van Der Helm. “Human motion control”. In: *Reader for Delft Course wb2407* January (2008). URL: http://stiff-project.eu/fileadmin/biomechanics/HMC{_}Reader.pdf.

[15] Terrence C Stewart. “A Technical Overview of the Neural Engineering Framework”. In: *The Newsletter of the Society for the Study of Artificial Intelligence and Simulation of Behaviour* 135.135 (2012), pp. 1–8.

[16] Valentin Senft et al. “Inhibiting basal ganglia regions reduces syllable sequencing errors in parkinson’s disease: A computer simulation study”. In: *Frontiers in Computational Neuroscience* 12.June (2018), pp. 1–13. ISSN: 16625188. DOI: 10.3389/fncom.2018.00041.

[17] Niels Taatgen. “A Spiking Neural Architecture that Learns New Tasks”. In: (2012).

[18] Christian Duval et al. “A brain network model explaining tremor in Parkinson’s disease”. In: *Neurobiology of Disease* 85 (2016), pp. 49–59. ISSN: 1095953X. DOI: 10.1016/j.nbd.2015.10.009. URL: http://dx.doi.org/10.1016/j.nbd.2015.10.009.

[19] Christopher H Chen et al. “Short latency cerebellar modulation of the basal ganglia”. In: 17.12 (2015), pp. 1767–1775. DOI: 10.1038/nn.3868.Short.

[20] Trenton Kriete et al. “Indirection and symbol-like processing in the prefrontal cortex and basal ganglia”. In: *Proceedings of the National Academy of Sciences of the United States of America* 110.41 (2013), pp. 16390–16395. ISSN: 00278424. DOI: 10.1073/pnas.1303547110.

[21] Terrence C. Stewart, Xuan Choo, and Chris Eliasmith. “Dynamic behaviour of a spiking model of action selection in the basal ganglia”. In: *Proceedings of the 10th International Conference on Cognitive Modeling, ICCM 2010* (2010), pp. 235–240.

[22] Chris Eliasmith et al. “A large-scale model of the functioning brain”. In: *Science* 338.6111 (2012), pp. 1202–1205. ISSN: 10959203. DOI: 10.1126/science.1225266.

[23] Andreas J. Keller, Morgane M. Roth, and Massimo Scanziani. “Neurons in Visual Cortex are Driven by Feedback Projections when their Feedforward Sensory Input is Missing”. In: *bioRxiv* (2020), pp. 1–37.

[24] Andreas J. Keller, Morgane M. Roth, and Massimo Scanziani. “Feedback generates a second receptive field in neurons of the visual cortex”. In: *Nature* 582.7813 (2020), pp. 545–549. ISSN: 14764687. DOI: 10.1038/s41586-020-2319-4. URL: http://dx.doi.org/10.1038/s41586-020-2319-4.

[25] Arend L. Schwab. “Multibody dynamics”. In: *Technische Universiteit Delft* (2018). ISSN: 15289036. DOI: 10.1115/1.3167189.

[26] David A. Winter. *Biomechanics and Motor Control of Human Movement: Fourth Edition*. 2009, pp. 1–370. ISBN: 9780470398180. DOI: 10.1002/9780470549148.

[27] Reza Shadmehr and Michael A. Arbib. “A mathematical analysis of the force-stiffness characteristics of muscles in control of a single joint system”. In: *Biological Cybernetics* 66.6 (1992), pp. 463–477. ISSN: 03401200. DOI: 10.1007/BF00204111.

[28] Michael Dimitriou. “Enhanced Muscle Afferent Signals during Motor Learning in Humans”. In: *Current Biology* 26.8 (2016), pp. 1062–1068. ISSN: 09609822. DOI: 10.1016/j.cub.2016.02.030. URL: http://dx.doi.org/10.1016/j.cub.2016.02.030.

[29] T. S. Buchanan. “Evidence that maximum muscle stress is not a constant: differences in specific tension in elbow flexors and extensors”. In: *Medical Engineering and Physics* 17.7 (1995), pp. 529–536. ISSN: 13504533. DOI: 10.1016/1350-4533(95)00005-8.

[30] Steven L. Peterson and Ghazi M. Rayan. “Shoulder and upper arm muscle architecture”. In: *Journal of Hand Surgery* 36.5 (2011), pp. 881–889. ISSN: 03635023. DOI: 10.1016/j.jhsa.2011.01.008. URL: http://dx.doi.org/10.1016/j.jhsa.2011.01.008.

[31] David Cofer et al. “AnimatLab: A 3D graphics environment for neuromechanical simulations”. In: *Journal of Neuroscience Methods* 187.2 (2010), pp. 280–288. ISSN: 01650270. DOI: 10.1016/j.jneumeth.2010.01.005. URL: http://dx.doi.org/10.1016/j.jneumeth.2010.01.005.

[32] Politi Antonio. “Dynamics of Networks of Leaky-Integrate-and-Fire Neurons”. In: *Network Science: Complexity in Nature and Technology* August (2010), pp. 1–27. DOI: 10.1007/978-1-84996-396-1.

[33] Chris Eliasmith and Charles H. Anderson. *Neural Engineering*. Ed. by TLFeBOOK. Vol. (5)2. 2. 2003. ISBN: 0262050714.

[34] Craig Citro Ashish Agarwal, Paul Barham, Eugene Brevdo, Zhifeng Chen. {*TensorFlow*}: *Large-Scale Machine Learning on Heterogeneous Systems*. URL: https://www.tensorflow.org/.

[35] Yong Yu et al. “A Review of Recurrent Neural Networks: LSTM Cells and Network Architectures Yong”. In: *Neural Computation* 31 (2019), pp. 1235–1270. DOI: 10.1162/NECO. arXiv: 1803.01446. URL: http://arxiv.org/abs/1803.01446.

[36] E. Knudsen. “Computational Maps In The Brain”. In: *Annual Review of Neuroscience* 10.1 (1987), pp. 41–65. ISSN: 0147006X. DOI: 10.1146/annurev.neuro.10.1.41.

[37] Arjan Boonman and Hans Ulrich Schnitzler. “Frequency modulation patterns in the echolocation signals of two vespertilionid bats”. In: *Journal of Comparative Physiology A: Neuroethology, Sensory, Neural, and Behavioral Physiology* 191.1 (2005), pp. 13–21. ISSN: 03407594. DOI: 10.1007/s00359-004-0566-8.

[38] Erika Kropf et al. “From anatomy to function: the role of the somatosensory cortex in emotional regulation”. In: *Revista brasileira de psiquiatria (Sao Paulo, Brazil : 1999)* 41.3 (2019), pp. 261–269. ISSN: 1809452X. DOI: 10.1590/1516-4446-2018-0183.

[39] Michael Brecht. “The Body Model Theory of Somatosensory Cortex”. In: *Neuron* 94.5 (2017), pp. 985–992. ISSN: 10974199. DOI: 10.1016/j.neuron.2017.05.018. URL: http://dx.doi.org/10.1016/j.neuron.2017.05.018.

[40] Gabriel Rilling, Patrick Flandrin, and Paulo Goncalves. “On empirical mode decomposition and its algorithms”. In: *IEEE-EURASIP workshop on nonlinear signal and image processing* 3 (2003), pp. 8–11.

[41] Ashish Bansal and Ajay Kumar. “Heisenberg uncertainty inequality for Gabor transform”. In: *Journal of Mathematical Inequalities* 10.3 (2016), pp. 737–749. ISSN: 1846579X. DOI: 10.7153/jmi-10-60. arXiv: 1507.00446.

[42] Hiroshi Asanuma. “Functional role of sensory inputs to the motor cortex”. In: *Progress in Neurobiology* 16 (1981), pp. 241–262.

[43] Lawrence C. Udeigwe, Paul W. Munro, and G. Bard Ermentrout. “Emergent Dynamical Properties of the BCM Learning Rule”. In: *Journal of Mathematical Neuroscience* 7.1 (2017). ISSN: 21908567. DOI: 10.1186/s13408-017-0044-6. URL: http://dx.doi.org/10.1186/s13408-017-0044-6.

[44] Peter Dayan et al. “The misbehavior of value and the discipline of the will”. In: *Neural Networks* 19.8 (2006), pp. 1153–1160. ISSN: 08936080. DOI: 10.1016/j.neunet.2006.03.002.

[45] Tiago V. Maia. “Reinforcement learning, conditioning, and the brain: Successes and challenges”. In: *Cognitive, Affective and Behavioral Neuroscience* 9.4 (2009), pp. 343–364. ISSN: 15307026. DOI: 10.3758/CABN.9.4.343.

[46] Hannah M. Bayer and Paul W. Glimcher. “Midbrain dopamine neurons encode a quantitative reward prediction error signal”. In: *Neuron* 47.1 (2005), pp. 129–141. ISSN: 08966273. DOI: 10.1016/j.neuron.2005.05.020.

[47] Jiping He and Stephen I.Helms Tillery. “Determining natural arm configuration along a reaching trajectory.” In: *Experimental brain research.* 167.3 (2005), pp. 352–361. ISSN: 00144819. DOI: 10.1007/s00221-005-0039-5.

[48] S Grossberg and R W Paine. “2000 Special Issue A neural model of cortico-cerebellar interactions during attentive imitation and predictive learning of sequential handwriting movements”. In: 13 (2000), pp. 999–1046.

[49] Paolo Viviani and Tamar Flash. “Minimum-Jerk, Two-Thirds Power Law, and Isochrony: Converging Approaches to Movement Planning”. In: *Journal of Experimental Psychology: Human Perception and Performance* 21.1 (1995), pp. 32–53. ISSN: 00961523. DOI: 10.1037/0096-1523.21.1.32.

[50] Chigozie Nwankpa et al. “Activation Functions: Comparison of trends in Practice and Research for Deep Learning”. In: (2018), pp. 1–20. arXiv: 1811.03378. URL: http://arxiv.org/abs/1811.03378.

[51] K. Gurney, T. J. Prescott, and P. Redgrave. “A computational model of action selection in the basal ganglia. II. Analysis and simulation of behaviour”. In: *Biological Cybernetics* 84.6 (2001), pp. 411–423. ISSN: 03401200. DOI: 10.1007/PL00007985.

[52] Valentin Senft et al. “Reduction of dopamine in basal ganglia and its effects on syllable sequencing in speech: A computer simulation study”. In: *Basal Ganglia* 6.1 (2016), pp. 7–17. ISSN: 22105336. DOI: 10.1016/j.baga.2015.10.003. URL: http://dx.doi.org/10.1016/j.baga.2015.10.003.

[53] K. Gurney, T. J. Prescott, and P. Redgrave. “A computational model of action selection in the basal ganglia. I. A new functional anatomy”. In: *Biological Cybernetics* 84.6 (2001), pp. 401–410. ISSN: 03401200. DOI: 10.1007/PL00007984.

[54] Mechelle M. Lewis et al. “The role of the cerebellum in the pathophysiology of Parkinson’s disease”. In: *The Canadian journal of neurological sciences. Le journal canadien des sciences neurologiques* 40.3 (2013), pp. 299–306. ISSN: 03171671. DOI: 10.1017/S0317167100014232.

[55] Tao Wu and Mark Hallett. “The cerebellum in Parkinson’s disease”. In: *Brain* 136.3 (2013), pp. 696–709. ISSN: 14602156. DOI: 10.1093/brain/aws360.

[56] THOMAS WICHMANN and MAHLON R. DeLONG. “Pathophysiology of Parkinson’s Disease: The MPTP Primate Model of the Human Disorder”. In: *Annals of the New York Academy of Sciences* 991.1 (2006), pp. 199–213. ISSN: 1749-6632. DOI: 10.1111/j.1749-6632.2003.tb07477.x.

[57] Alexander Blenkinsop, Sean Anderson, and Kevin Gurney. “Frequency and function in the basal ganglia: the origins of beta and gamma band activity”. In: *Journal of Physiology* 595.13 (2017), pp. 4525–4548. ISSN: 14697793. DOI: 10.1113/JP273760.

[58] G. Du et al. “Properties of oscillatory neuronal activity in the basal ganglia and thalamus in patients with Parkinson’s disease”. In: *Translational Neurodegeneration* 7.1 (2018), pp. 1–13. ISSN: 20479158. DOI: 10.1186/s40035-018-0123-y.

[59] Anne B. Young Roger L. Albin and John B. Penney. “The functional anatomy of basal ganglia disorders”. In: *Perspectives on disease* 12.10 (1989), pp. 366–374. ISSN: 14657333. DOI: 10.1093/jhered/esy024.

[60] Michiel F. Dirkx et al. “Dopamine controls Parkinson’s tremor by inhibiting the cerebellar thalamus”. In: *Brain* 140.3 (2017), pp. 721–734. ISSN: 14602156. DOI: 10.1093/brain/aww331.

[61] Jesse Read et al. “Classifier chains for multi-label classification”. In: *Machine Learning* 85.3 (2011), pp. 333–359. ISSN: 08856125. DOI: 10.1007/s10994-011-5256-5.

[62] Nitesh V. Chawla et al. “SMOTE: Synthetic minority over-sampling technique”. In: *Journal of Artificial Intelligence Research* 16 (2002), pp. 321–357. ISSN: 10769757. DOI: 10.1613/jair.953. arXiv: 1106.1813.

[63] H. Bergman et al. “The primate subthalamic nucleus. II. Neuronal activity in the MPTP model of parkinsonism”. In: *Journal of Neurophysiology* 72.2 (1994), pp. 507–520. ISSN: 00223077. DOI: 10.1152/jn.1994.72.2.507.

[64] Atsushi Nambu et al. “Excitatory conical inputs to pallidal neurons via the subthalamic nucleus in the monkey”. In: *Journal of Neurophysiology* 84.1 (2000), pp. 289–300. ISSN: 00223077. DOI: 10.1152/jn.2000.84.1.289.

[65] Mohammad Daneshzand, Miad Faezipour, and Buket D. Barkana. “Hyperbolic Modeling of Subthalamic Nucleus Cells to Investigate the Effect of Dopamine Depletion”. In: *Computational Intelligence and Neuroscience* 2017 (2017). ISSN: 16875273. DOI: 10.1155/2017/5472752.

[66] Cyril Dejean et al. “Dynamic changes in the cortex-basal ganglia network after dopamine depletion in the rat”. In: *Journal of Neurophysiology* 100.1 (2008), pp. 385–396. ISSN: 00223077. DOI: 10.1152/jn.90466.2008.

[67] Lars Timmermann et al. “The cerebral oscillatory network of parkinsonian resting tremor”. In: *Brain* 126.1 (2003), pp. 199–212. ISSN: 00068950. DOI: 10.1093/brain/awg022.

[68] Nima Dehghani and Ralf D. Wimmer. “A computational perspective of the role of the thalamus in cognition”. In: *Neural Computation* 31.7 (2019), pp. 1380–1418. ISSN: 1530888X. DOI: 10.1162/neco_a_01197. arXiv: 1803.00997.

[69] Marife Arancillo et al. “In vivo analysis of purkinje cell firing properties during postnatal mouse development”. In: *Journal of Neurophysiology* 113.2 (2015), pp. 578–591. ISSN: 15221598. DOI: 10.1152/jn.00586.2014.

[70] Anders Rasmussen et al. “Changes in complex spike activity during classical conditioning”. In: *Frontiers in Neural Circuits* 8.AUG (2014), pp. 1–13. ISSN: 16625110. DOI: 10.3389/fncir.2014.00090.

[71] Yaara Lefler, Benjamin Torben-Nielsen, and Yosef Yarom. “Oscillatory activity, phase differences and phase resetting in the inferior olivary nucleus”. In: *Frontiers in Systems Neuroscience* 7.MAY (2013). ISSN: 16625137. DOI: 10.3389/fnsys.2013.00022.

[72] Sarah Gebai et al. “Tremor reduction at the palm of a parkinson’s patient using dynamic vibration absorber”. In: *Bioengineering* 3.3 (2016). ISSN: 23065354. DOI: 10.3390/bioengineering3030018.

[73] William C. Koller, Karen Busenbark, and Kevin Miner. “The relationship of essential tremor to other movement disorders: Report on 678 patients”. In: *Annals of Neurology* 35.6 (1994), pp. 717–723. ISSN: 15318249. DOI: 10.1002/ana.410350613.

[74] Elan D. Louis et al. “Clinical correlates of action tremor in Parkinson disease”. In: *Archives of Neurology* 58.10 (2001), pp. 1630–1634. ISSN: 00039942. DOI: 10.1001/archneur.58.10.1630.

[75] Seong Beom Koh et al. “Dissociation of Cardinal Motor signs in Parkinson’s disease patients”. In: *European Neurology* 63.5 (2010), pp. 307–310. ISSN: 00143022. DOI: 10.1159/000314179.

[76] Christian Duval et al. “The impact of ventrolateral thalamotomy on tremor and voluntary motor behavior in patients with Parkinson’s disease”. In: *Experimental Brain Research* 170.2 (2006), pp. 160–171. ISSN: 00144819. DOI: 10.1007/s00221-005-0198-4.

[77] Jeffrey D. Atkinson et al. “Optimal location of thalamotomy lesions for tremor associated with Parkinson disease: A probabilistic analysis based on postoperative magnetic resonance imaging and an integrated digital atlas”. In: *Journal of Neurosurgery* 96.5 (2002), pp. 854–866. ISSN: 00223085. DOI: 10.3171/jns.2002.96.5.0854.

[78] Omar Mamad et al. “Dopaminergic control of the globus pallidus through activation of D2 receptors and its impact on the electrical activity of subthalamic nucleus and substantia nigra reticulata neurons”. In: *PLoS ONE* 10.3 (2015), pp. 1–16. ISSN: 19326203. DOI: 10.1371/journal.pone.0119152.

[79] Luka Milosevic et al. “Physiological mechanisms of thalamic ventral intermediate nucleus stimulation for tremor suppression”. In: *Brain* 141.7 (2018), pp. 2142–2155. ISSN: 14602156. DOI: 10.1093/brain/awy139.

[80] John R. Huguenard and David A. McCormick. “Thalamic synchrony and dynamic regulation of global forebrain oscillations”. In: *Trends in Neurosciences* 30.7 (2007), pp. 350–356. ISSN: 01662236. DOI: 10.1016/j.tins.2007.05.007.

[81] Takao Hashimoto et al. “Stimulation of the subthalamic nucleus changes the firing pattern of pallidal neurons”. In: *Journal of Neuroscience* 23.5 (2003), pp. 1916–1923. ISSN: 02706474. DOI: 10.1523/jneurosci.23-05-01916.2003.

[82] R. R. Llinás. “Inferior olive oscillation as the temporal basis for motricity and oscillatory reset as the basis for motor error correction”. In: *Neuroscience* 162.3 (2009), pp. 797–804. ISSN: 03064522. DOI: 10.1016/j.neuroscience.2009.04.045. URL: http://dx.doi.org/10.1016/j.neuroscience.2009.04.045.

[83] Mario Negrello et al. *Quasiperiodic rhythms of the inferior olive*. Vol. 15. 5. 2019, pp. 1–41. ISBN: 1111111111. DOI: 10.1371/journal.pcbi.1006475.

Supplementary Materials

Tables

Table 1: *Links parameters: m mass, l length and $I = \frac{ml^2}{12}$ momentum of inertia [26].*

–	Upper arm	Lower arm
$m\,[Kg]$	2.24	1.28
$l\,[m]$	0.335	0.263
$I\,[Kg\,m^2]$	0.021	0.0074

Table 2: *Joint friction parameters: K joint stiffness, β joint viscosity.*

–	Shoulder Joint	Elbow Joint
$K\,[\frac{N}{rad}]$	1.7	1.7
$\beta\,[\frac{N}{rads}]$	2.1	2.1

Table 3: *l_0 resting length, r-d distance of the attachment point to the right-left of the related joint. k_{pe} muscle parallel stiffness, k_{se} tendon stiffness, β_{pe} muscle parallel viscosity, k_p spindle stiffness, k_v spindle viscosity, k_f GTO multiplicative factor, l_w breadth of length-tension relationship, PCSA physiological cross-sectional area, σ_{max} maximal tension [30, 26]*

–	Anterior Deltoid	Posterior Deltoid	Biceps	Triceps
$l_0\,[m]$	0.049	0.06	0.32	0.305
$r\,[m]$	0.03	0.041	0.038	0.04
$d\,[m]$	0.02	0.03	0.3	0.285
$k_{pe}\,[\frac{N}{m}]$	400	400	300	300
$k_{se}\,[\frac{N}{m}]$	10 000	10 000	8000	8000
$\beta_{pe}\,[\frac{N}{ms}]$	30	30	20	20
$k_p\,[\frac{N}{m}]$	117	117	117	117
$k_v\,[\frac{N}{ms}]$	33	33	33	33
$k_f\,[\,]$	0.35	0.35	0.35	0.35
$l_w\,[m]$	0.3	0.3	0.3	0.3
PCSA $[cm^2]$	10	6	5	8
$\sigma_{max}\,[\frac{N}{cm^2}]$	80	40	80	40
Feedback Type	Position	Velocity	Force	Visual
$\tau\,[ms]$	30	20	20	10

, τ feedback time delay.

TMT method

In order to obtain Eq. 1 the following quantities are calculated: First, the inertia matrix is expressed by

$$\mathbf{M} = \begin{bmatrix} m_1 & 0 & 0 & 0 & 0 & 0 \\ 0 & m_1 & 0 & 0 & 0 & 0 \\ 0 & 0 & I_1 & 0 & 0 & 0 \\ 0 & 0 & 0 & m_2 & 0 & 0 \\ 0 & 0 & 0 & 0 & m_2 & 0 \\ 0 & 0 & 0 & 0 & 0 & I_2 \end{bmatrix}$$

while the transformation matrix T is determined by the partial derivative of the the $\mathbf{x} = [X_{O_1}, Y_{O_1}, \Theta_{O_1}, X_{O_2}, Y_{O_2}, \Theta_{O_2}]$ w.r.t. the generalized coordinates $\mathbf{q}$.

$$\mathbf{T} = \frac{\partial \mathbf{x}}{\partial \mathbf{q}} = \begin{bmatrix} -\frac{l_1}{2} sin(\theta_1) & 0 \\ \frac{l_1}{2} cos(\theta_1) & 0 \\ 1 & 0 \\ -l_1 sin(\theta_1) & -\frac{l_2}{2} sin(\theta_2) \\ l_1 cos(\theta_1) & \frac{l_2}{2} cos(\theta_2) \\ 0 & 1 \end{bmatrix} \tag{11}$$

In order to reduce the inertia matrix and the force vector f (Eq. 5) to the generalized coordinates frame of reference

$$\mathbf{f} = \begin{bmatrix} 0 \\ m_1 g \\ T_{1f} - T1e + s_f \\ 0 \\ m_2 g \\ T_{2f} - T2e + e_f \end{bmatrix}$$

the reduced generalized force vector $\bar{\mathbf{Q}}$ is calculated through the use of the transformation matrix in the following way:

$$\bar{\mathbf{Q}} = \mathbf{Q} + \mathbf{T}^T(\mathbf{f} - \mathbf{M}\mathbf{g}) \tag{12}$$

The convolutional term g is calculated in the following way

$$\mathbf{g} = \frac{\partial^2 \mathbf{T}}{\partial \mathbf{q^2}} = \begin{bmatrix} -\frac{l_1 cos(\theta_1)\dot{\theta_1^2}}{2} \\ -\frac{l_1 sin(\theta_1)\dot{\theta_1^2}}{2} \\ 0 \\ -l_1 cos(\theta_1)\dot{\theta_1^2} - \frac{l_2 cos(\theta_2)\dot{\theta_2^2}}{2} \\ -l_1 sin(\theta_1)\dot{\theta_1^2} - \frac{l_2 sin(\theta_2)\dot{\theta_2^2}}{2} \\ 0 \end{bmatrix}$$

and the term $\mathbf{Q} = 0$ correspond to the applied external forces. The reduced inertia matrix $\bar{\mathbf{M}} = \mathbf{T^T M T}$ is then used to compute Eq. 1 together with the reduced force vector $\bar{\mathbf{Q}}$.

Extensive results

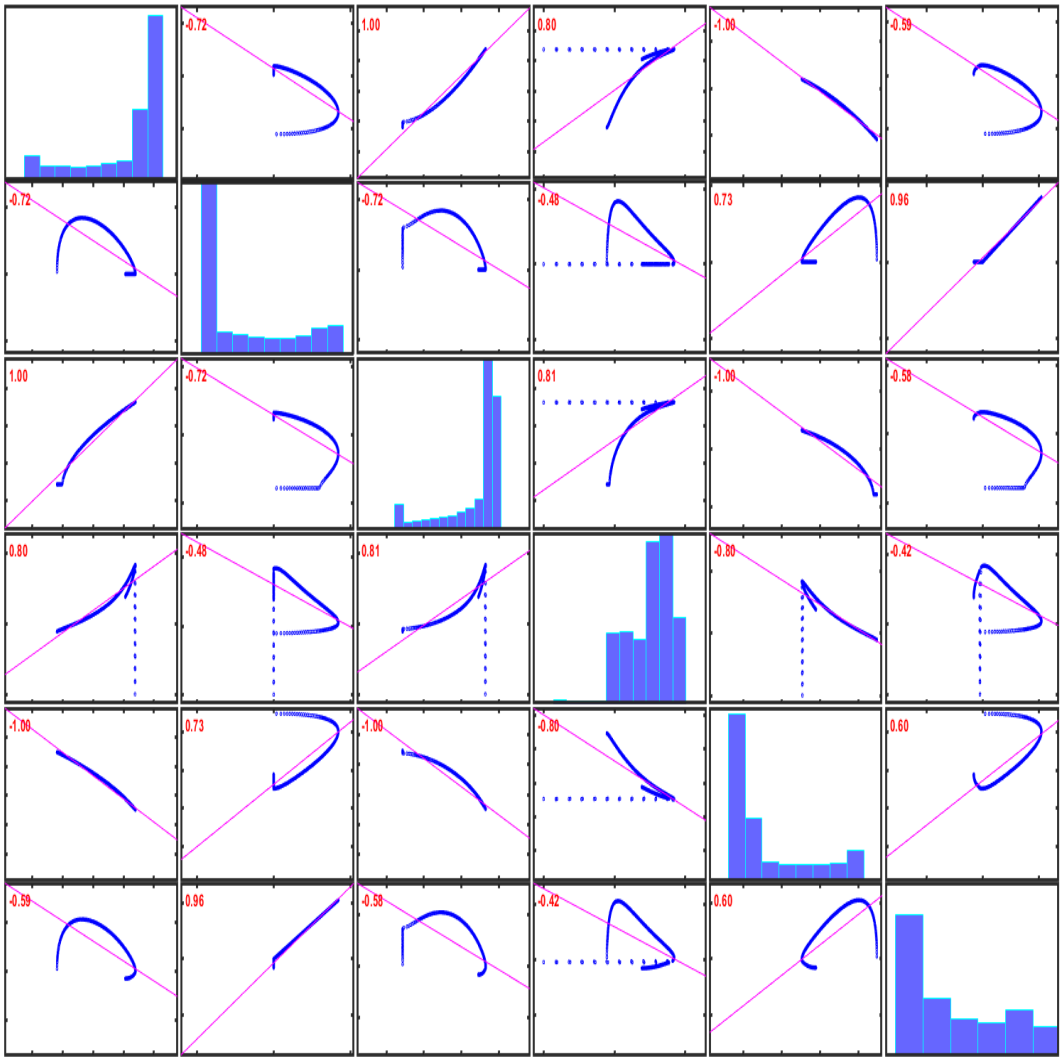

Figure 5.1: *Cross-correlogram of Anterior Deltoid state variables. In red the Spearman ρ, P<0.01. From left to right: length, velocity feedback, position feedback, force, angle α, elongation w.r.t. resting length.*

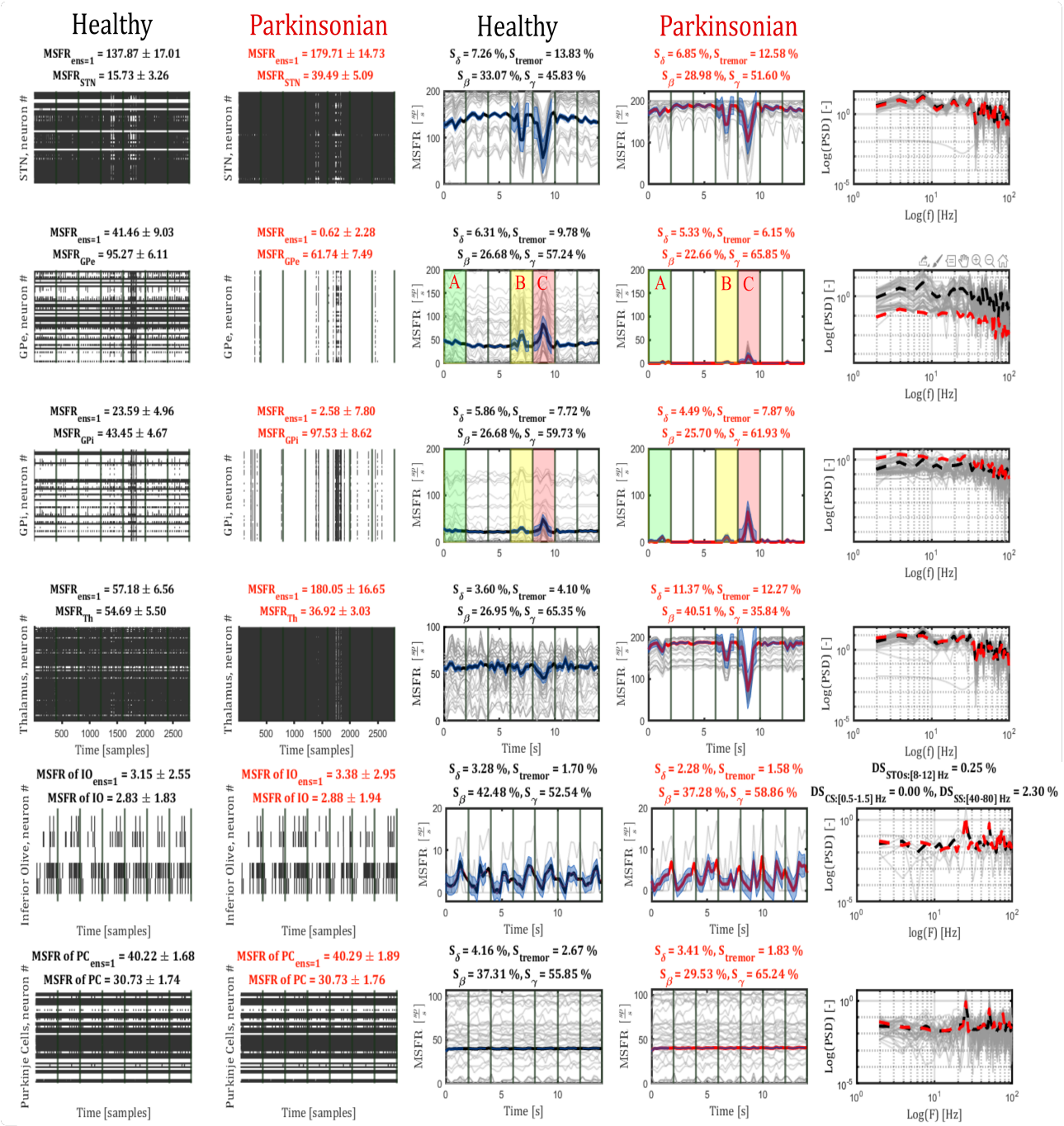

Figure 5.2: ***Left****: Raster plots of the neurons in one ensemble ($N_{ens} = 1$ for the BG-TH loop and $N_{ens} = 1$ for IO-PC).* ***Center****: Mean spike rate averaged over a temporal bin of $250\,ms$ of the sample ensemble shown the left. In clear black (healthy) and red (PD) the mean over all the ensembles and over all neurons in the ensembles of the mean spiking frequency and in shaded blue the related standard deviation. With the same colors of Fig. 11, the three areas of main activity of the GPi and GPe.* ***Right****: Healthy subject spectrogram (after windowing with Tukey window $cosine_{fraction} = 0.25$) of all neurons in the ensemble shown on the left. With dashed lines the averaged power of the ensemble for the healthy (black) and the PD condition (red).* ***All****: The cumulative statistics, as mean firing frequency of the neural area or the mean spectral power are calculated on all the clustered trajectories in the dataset, while the raster plot and the mean spike rate are shown only for clusters $n_{clusters} = 1, 2, ..., 7$. The dopamine values for the PD simulation were set to $l_g = l_e = 0$.*

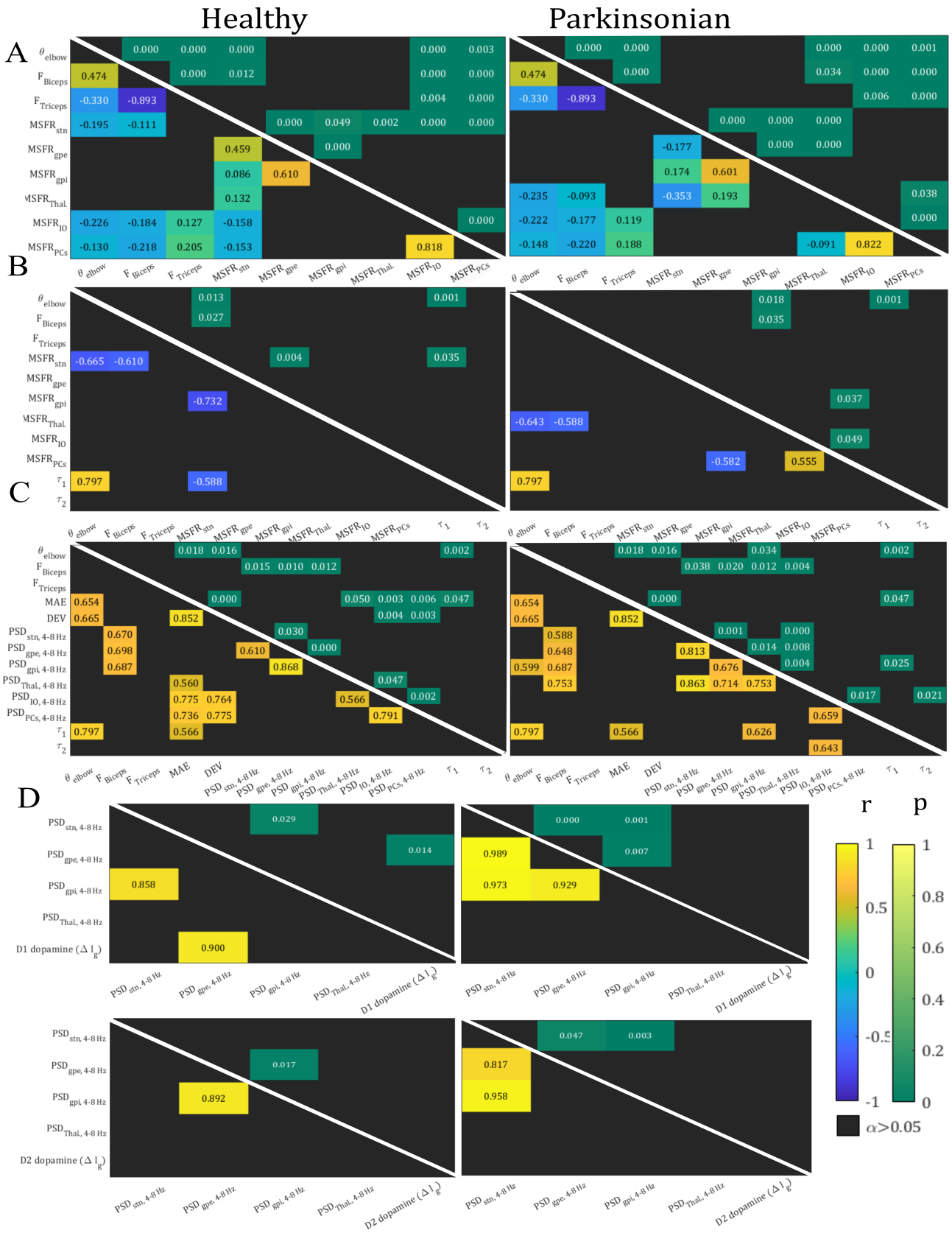

Figure 5.3: ***A****: Spearman ρ between MSFR of BG-TH-CBLM areas and kinematic-dynamic variables. Calculated using re-sampled data with bin size of 250 ms as in 5.2.* ***B****: Spearman ρ between MSFR of BG-TH-CBLM areas and kinematics-dynamics variables. Calculated per each trajectory.* ***C****: Correlation between PSD of the tremor band, MAE and STD of the trajectory prediction and kinematic-dynamic variables.* ***D****: Correlation between PSD of the tremor band, D1 dopamine (left) and D2 dopamine (right) variation.* ***All****: The lower triangular side represents the ρ while the upper triangular side the p. In black, correlations with $P > 0.05$.*